EVALUATING ASTER AND WORLDVIEW-3 MINERAL MAPPING CAPABILITIES IN AN EPITHERMAL ALTERATION SYSTEM

Musa Shehu Usman
March, 2018

SUPERVISORS:
Dr. Harald van der Werff
Dr. Rob Hewson

EVALUATING ASTER AND WORLDVIEW-3 MINERAL MAPPING CAPABILITIES IN AN EPITHERMAL ALTERATION SYSTEM

Musa Shehu Usman
Enschede, The Netherlands, March, 2018

Thesis submitted to the Faculty of Geo-Information Science and Earth Observation of the University of Twente in partial fulfilment of the requirements for the degree of Master of Science in Geo-Information Science and Earth Observation.
Specialization: Applied Earth Sciences – Geological Remote Sensing

SUPERVISORS:
Dr. Harald van der Werff
Dr. Rob Hewson

THESIS ASSESSMENT BOARD:
Prof. dr. F.D. van der Meer (Chair)
Dr. M. Schodlok [External Examiner, Federal Institution for Geosciences and Natural Resources, (Germany)]

ABSTRACT

The inactivation of the Advanced Spaceborne Thermal Emission and Reflection Radiometer (ASTER) shortwave (SWIR) detector that is widely used for geologic remote sensing applications has posed a problem to the geological community. This research aimed at comparing the ASTER's capabilities with the new multispectral Worldview-3 sensor towards providing data continuity for the ASTER. Images of the sensors were collected at different times over an epithermal alteration system in Rodalquilar, southeast Spain. HyMAP data was used to simulate both sensors in order to correct for the temporal difference. A band ratio approach using two different sets of algorithms were analysed with scatter plots. Kaolinite, AlOH, MgOH, ferrous iron content in MgOH/carbonate, jarosite and siderite indices were used for the comparison. Indices made with ASTER appeared to be noisy and less intense in discriminating the mineralogy of the study area. Worldview-3 interpretations, in comparison to ASTER, show patterns that are much more spatially coherent with lithologies in the published geological map of the area. Differences in mineral abundance of kaolinite and AlOH, less in May and more in September, were noticed. Jarosite, on the other hand, was more abundant in May than in September. The scatter plots of ASTER versus Worldview-3 and between the two scenes of Worldview-3 also confirmed the difference in the interpretations of the index products in the images. Overall, the results show that WV-3 at 7.5m spatial resolution discriminate the indices product better than ASTER at 30m. Therefore, WV-3 can provide data continuity for ASTER SWIR geological capabilities. Kaolinite, AlOH and jarosite are sensitive to seasonal changes while MgOH and ferrous iron content in MgOH/carbonate are less sensitive.

ACKNOWLEDGEMENTS

"*Alhamdu Lillahi Rabbil Alamin bi niimatihi tatummul solihaat.*"

The Joint Japan World Bank Graduate Scholarship Programme (JJWGSP) facilitated my study at the prestigious faculty for Geo-Information Science and Earth Observation (ITC), University of Twente, The Netherlands, by offering a full scholarship for the programme. I remained grateful to the JJWGSP. My gratitude goes to my entire family for their understanding and encouragement during the programme.

I am indebted to my supervisors Dr. Harald van der Werff and Dr. Rob Hewson for their constructive criticisms and stimulation before and during the research, and also to the course director Mr. Bart Krol for his guidance, support and encouragement throughout the programme. Professor Freek van der Meer, your Chairmanship style is a stimulus for scientific research. To the entire staff, I say a big thank you.

Importantly, I wish to express my appreciation to the Digital Globe for providing the two scenes of WV-3 data coverage of Rodalquilar that was used in this research, Mr. Dan Taranik (Exploration Mapping Group inc.), the facilitator of the great gift. Also, to the NASA/LPDAAC/USGS for access to the free the ASTER data coverage of the study area.

I am also grateful for information and assistance from the staff at the Cabo de Gata Nijar National Park Office, Rodalquilar, to my ITC colleagues and myself.

My colleagues in the geological remote sensing you are wonderful, my friend from other domains and back home you are wonderful.

TABLE OF CONTENTS

LIST OF FIGURES

LIST OF TABLES

1. INTRODUCTION

1.1. Background

Sensors used in imaging spectroscopy have different capabilities in obtaining earth surface information. The instrumental design of every sensor affects its observed response within the various electromagnetic regions. Key factors in the design are sensor tradeoff between the spectral and spatial resolutions, and the signal to noise ratio (Mookambiga & Gomathi, 2016). The striking characteristics of sensors include spatial and spectral coverage. The sensors are usually designed to serve for generic or some particular application. For instance, HyMAP, an airborne hyperspectral scanner with 126 contiguous bands can be used in almost all applications, while Advance Space Thermal Emission and Reflection Radiometer (ASTER) is intended for predominantly geological remote sensing, and the WorldView-3 (WV-3) is also intended for both geological and environmental studies. The spectral resolution is critical for identifying materials while the spatial resolution is important for locating objects (Mookambiga & Gomathi, 2016). Figure 1.1 shows each band's position on the electromagnetic spectrum of ASTER, WV-3 and HyMAP, that will be used in this research.

Multispectral sensors are satellite-based detectors that measure reflected energy in multiple spectral bands across the electromagnetic spectrum. Although characterized by limited spectral resolution and spectral range (Kruse & Perry, 2009), they have been used for various geological studies since the beginning of remote sensing technology (van der Meer et al., 2012). Initial scanners include Landsat Multispectral Scanner (MSS) and Thematic Mapper (TM), and Advance Space Thermal Emission and Reflection Radiometer (ASTER). ASTER is considered to be an improvement on the initial 7-bands Landsat Thematic Mapper (Hewson & Cudahy, 2011; van der Meer et al., 2012). It has fourteen channels across the visible-near infrared (VNIR), shortwave infrared (SWIR) and thermal infrared (TIR) parts of the electromagnetic spectrum (Figure1 & Table1). Its SWIR has a channel that offers information from 2.360 - 2.430um. Right from inception in 1999, ASTER has been the default sensor for geological remote sensing applications (van der Meer et al., 2014 & 2012; van der Werff & van der Meer, 2015). In the year 2008, the SWIR detectors of ASTER malfunctioned, and the ASTER advisory of NASA publicly declared it non-operational in 2009. The SWIR data acquired since April 2008 became no longer usable except the other parts of the sensor. (https://asterweb.jpl.nasa.gov/swir-alert.asp).

Since the ASTER SWIR sensor has become non-operational, there is a need for data continuity of the ASTER capability for the geology community. The need for data continuity was emphasized by van der Meer et al. (2012). Researches for providing solution to aforementioned panic are ongoing; recent achievements include the work of van der Meer et al (2012) and van der Werff & van der Meer (2015). They studied and highlighted the geological capabilities of Sentinel-2.

In August 2015, the commercial multispectral sensor WorldView-3 operated by DigitalGlobe (https://www.digitalglobe.com/) was launched. The geological potential of the WV-3 sensor for alteration mineral mapping was simulated with AVIRIS data acquired in the Cuprite area (Kruse, Baugh, & Perry, 2015). The WorldView-3 (WV-3) sensor has 16 bands across the VNIR - SWIR wavelength range, it has 8 bands in the VNIR and 8 bands in the SWIR regions (Figure1 and Table1), 1.2m spatial resolution in the VNIR and 3.7 in the SWIR. For commercial delivery, however, the SWIR data resolution is down sampled to 7.5m. It is an extended version of the earlier WorldView-2 which as 8 bands in the VNIR, with an additional 8 SWIR bands. The SWIR 5, 6, 7 and 8 of the Worldview-3 are replicates of the ASTER SWIR bands design (Kruse and Perry 2013).

Datasets available for this research have temporal differences, ASTER acquired on 6th May 2004, two scenes of WV-3 acquired on 20th May & 9th September 2017, and HyMAP data acquired on 18th May 2004.

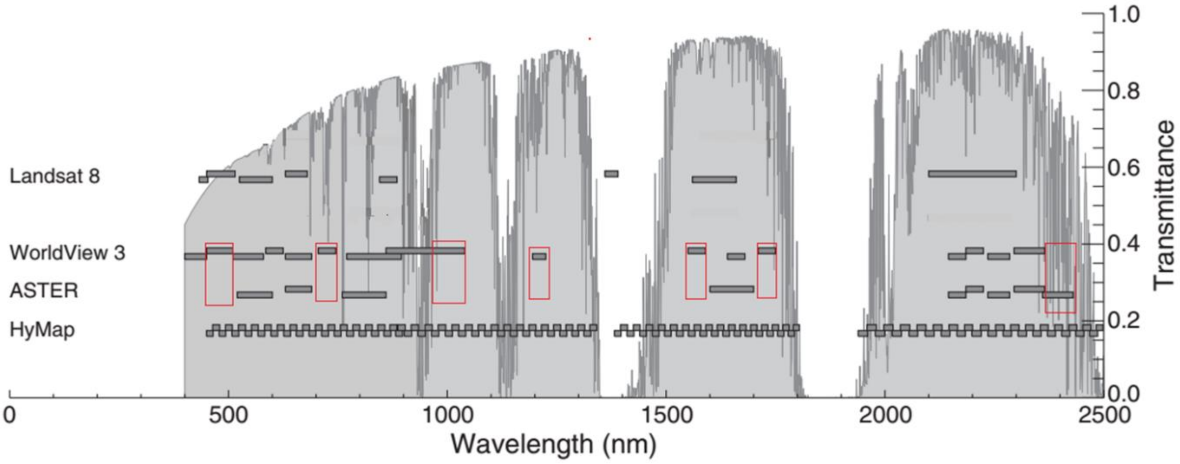

Figure 1.1 Model of the Atmospheric window showing the bands positions of Landsat 8, WV-3, ASTER and HyMAP across the VNIR-SWIR range of the electromagnetic spectrum (EMS) (modified after van der Werff and van der Meer et al, 2015). Red rectangles indicate band positions where ASTER and WV-3 differ.

Table 1.1 HyMap, WorldView-3 and ASTER specifications (Note: ***** Contiguous band, ****** Discrete band)

Property	HyMap*		WorldView-3**		ASTER**	
	VNIR	SWIR	VNIR	SWIR	VNIR	SWIR
Spectral	VIS:	S1:				
range(μm)	0.45 - 0.89	1.40 - 1.80	0.40 - 0.45	1.195 - 1.225	0.52 - 0.60	1.600 -1.700
	NIR:	S2:				
	0.89 - 1.35	1.95 - 2.48	0.45 – 0.51	1.550 - 1.590	2: 0.63 -0.69	2.145 -2.185
					N:	
			0.51 – 0.58	1.640 - 1.680	0.76 -0.86	2.185 -2.225
					B:	
			0.585 - 0.625	1.710 - 1.750	0.76 - 0.86	2.235 -2.285
			0.63 - 0.69	2.145 - 2.185		2.295 -2.365
			0.705 - 0.745	2.185 - 2.225		2.360 -2.430
			0.77 - 0.895	2.235 - 2.285		
			0.86 - 1.04	2.295 - 2.365		
Number of bands	126 (contiguous)		8 (discrete)	8 (discrete)	3 (discrete)	6 (discrete)
Spatial Resolution (m)	4		1.2	7.5	15	30

(Modified from Cocks et al., (1998); https://www.digitalglobe.com/; ASTER user handbook v2)

The SWIR region of EMS is an important region for mineral especially clay and carbonate mapping. Traditionally, ASTER in the series of multispectral sensors provides information in this region for geological mapping until 2008. However, the inactivation of this epic SWIR in ASTER has created an information void from the multispectral sensors since 2008, until WV-3 was launched in 2015. As pointed out by van der Werff and van der Meer (2015), studying a dynamic phenomenon will require time series data instead of only archived data thus, the need for ASTER SWIR data continuity is preferable, especially if the optimal daytime acquisition has yet to be collected. Several research have studied the geological capabilities of ASTER, and few published including the work of Sun et al (2016) and Kruse and Perry (2013) on WV-3 capabilities. To the knowledge of this research, no work has compared the geological capabilities of ASTER and WV-3.

1.2. Research objective

The main objective of this research is to compare ASTER with WV-3 for mineral mapping in a hydrothermal alteration system.

1.2.1 Sub – objectives

i. Compare the potential of WV-3 and ASTER band ratio products for alteration mineral mapping.
ii. Determine which of these sensors discriminate and identify which representative alteration minerals.
iii. Analyze the effect of seasonal differences (summer and spring) of the two WV-3 scenes, in terms of mineral and environmental mapping.

1.3. Research questions

i. Are there any minerals that are not discriminated and identified by ASTER but discriminated and identified by WV-3?
ii. Given the spectral and spatial resolutions trade-off, which of the sensors will be preferred for iron-bearing, clay, and carbonate minerals mapping?
iii. Does the spatial resolution of WV-3 make a difference in the mineral discrimination as compared to an ASTER image?
iv. Is any of the index product sensitive to seasonality, and do I need a particular season of the year for optimum identification of specific mineral product(s)?
v. Does the seasonal variation of the year affect the identification of alteration minerals from the same sensor?

1.4. Thesis structure

Chapter 1: Introduction, this include background, research objective and research questions.
Chapter 2: Description of the geographical location, climate and geology of the study area and the datasets used.
Chapter 3: Detailed description of methodology.
Chapter 4: Results of the images processing.
Chapter 5: Discussions on the findings from the image processing
Chapter 6: Conclusions recommendations.

2. STUDY AREA AND DATASET

2.1. Location and Geological settings

The study area (36˚ 50´N 2˚ 01´W) is part of the protected Cabo de Gata National Park, located at South-eastern Spain (Figure 2.1a), the aridest part of Europe and host to the Almeria – Cartagena volcanic belt (Figure 2.1b) (Oyarzun et al., 2009). The Cabo de Gata volcanic block (Figure 2.1b) is bounded on the northwest by the strike-slip fault and comprises series of volcanic rocks ranging from WSW to ENE (Arribas et al., 1995). The field comprises of calc-alkaline volcanism of Miocene (Rytuba et al., 1990). It is a combination of igneous processes and crustal contamination. Compositionally, the volcanic rocks range from pyroxene andesites to rhyolites(Arribas, 1995; Oyarzun et al., 2009; van der Meer, 2006). The volcanic field has several calderas including Los Frailes, Lomilla and Rodalquilar. The Rodalquilar caldera is typical of high sulfidation epithermal alteration systems (Figure2.1c).

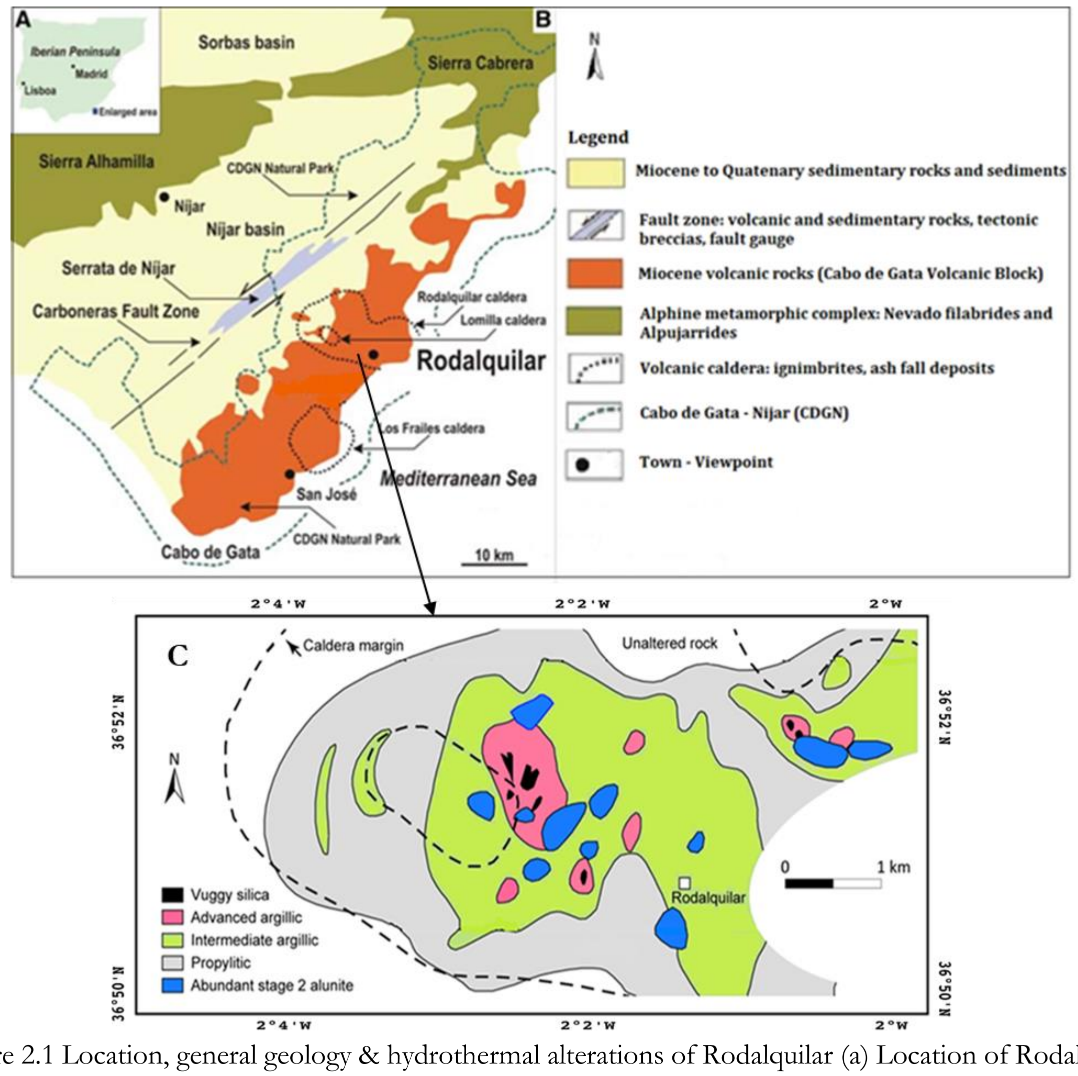

Figure 2.1 Location, general geology & hydrothermal alterations of Rodalquilar (a) Location of Rodalquilar in southeastern Spain. (b) General geology of the Almeria – Cartagena volcanic belt highlighting the regional geology of the Rodalquilar area (Modified after Oyarzun et al., 2009) (c) Five hydrothermal alteration zones that characterized Radaquilar epithermal high-sulfidation system (Modified from Arribas, 1995).

The Rodalquilar caldera is bounded on its northwestern axis by a strike-slip fault that resulted in Miocene calc-alkaline volcanic event (Figure 2.1b). It is an oval-shaped collapse structure characterized by coalescing stratovolcanoes and cones (Rytuba et al., 1990). The caldera is intensely hydrothermally altered and associated with gold – alunite and Pb-Zn-Ag-Au veins (Rytuba et al., 1990, Arribas et al., 1995b). The igneous activity in the caldera was accompanied by structural doming, fracturing and faulting which enhance the hydrothermal activities that formed the epithermal deposits (Arribas et al., 1995; Rytuba et al., 1990). It hosts the Rodalquilar gold deposit, the first documented example of caldera-related epithermal gold alunite mineralization in Europe (Bedini et al., 2009). The epithermal mineralization is associated with complex hydrothermal alteration assemblage, which characterized high-sulfidation systems (Arribas et al., 1995). Five high to low-temperature alteration zones (Fig 2.1c); silicic, advance argillic, intermediate argillic, propylitic and sericitic were distinguished (Arribas et al., 1995). The common minerals in these systems include alunite, kaolinite-dickite, illite, illite/smectite, jarosite, hematite, goethite, pyrite and pyrophyllite (Arribas et al, 1995). Regional subsidence below sea level after the last volcanic event in the area led to the deposition of shallow marine sediments in the western and eastern part (Arribas et al.,1995). Mining activities in Rodalguilar started since 1800 with the extraction of Pb, Zn and Cu then followed the discovery and mining of gold that lasted up to 1966.

2.2. Climate

The climate is typical of Mediterranean semi-arid with low annual rainfall and hot and dry summer. Oyarzun et al., 2009, described the weather with mean annual precipitation and temperature of 200mm and 18°C respectively. A thirty-year record (1960 – 1990) showed 2023 (±1000) mm average annual rainfall with minimum and maximum annual rates of 1020 and 5495 mm, respectively. Alonso-Sarria and López Bermúdez (1994) reported a concentration of the majority of the rainfall in the winter months (October to March) (Ferrier et al., 2009). The weather histories of the time of acquisitions of the images (appendix I-III) are collected from Almeria and Carboneras weather stations around the study area. https://www.wunderground.com/history/airport/LEAM/2017/10/6/MonthlyHistory.html?&reqdb.zip =&reqdb.magic=&reqdb.wmo= (Figure 2.2)

Figure 2.2 Location of Almeria and Carboneras weather stations indicated by red oval rings

The study area is characterized by varieties of perennial plants both photosynthetic and non-photosynthetic such as Esparto *Stipa tenacissima L.*, Palmito *Chamaerops humilis L.*, Albardin *Lygeum Spartum L.* (Figure 2.3) that pose a challenge to remote sensing studies.

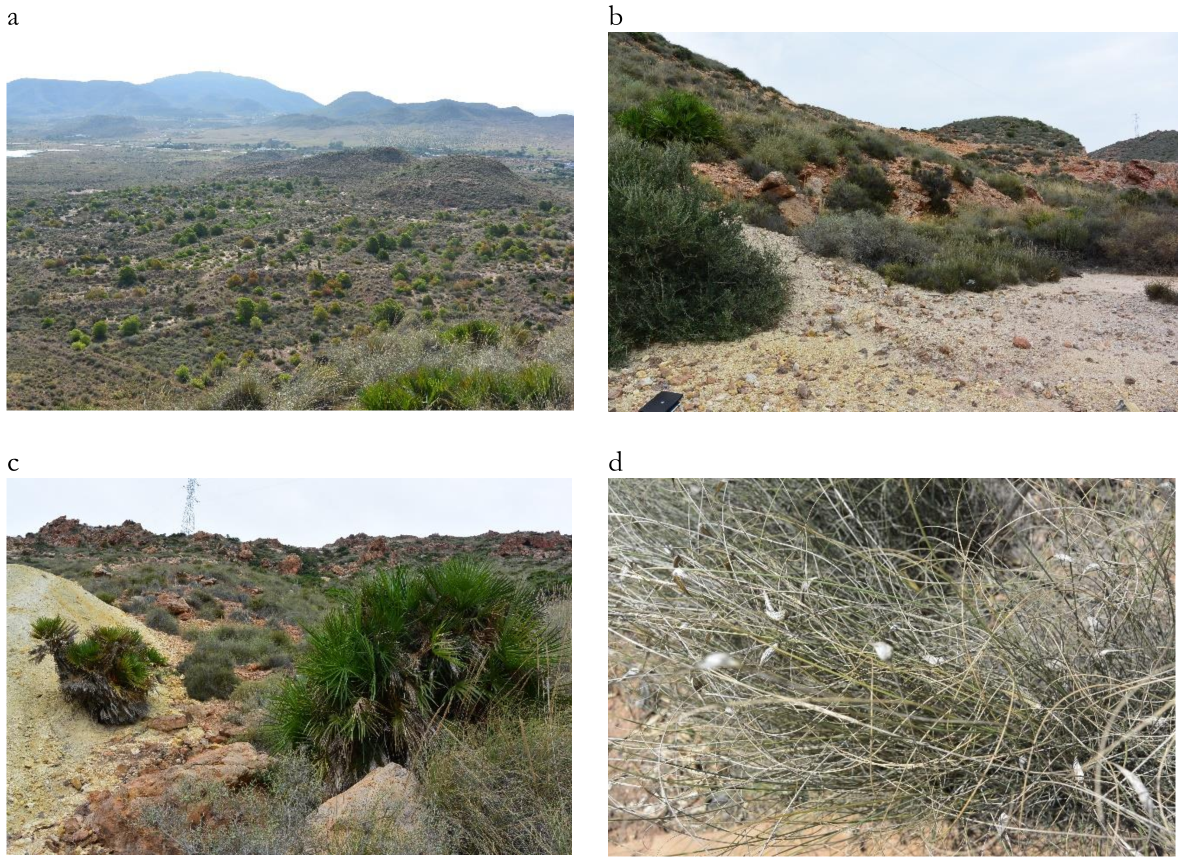

Figure 2.3 Spring view of Rodalquilar vegetation cover captured September 2017.

2.3. Datasets

Two multispectral (ASTER and WV-3) and one hyperspectral (HyMAP) sensors, LiDAR, field spectra collected with ASD and published alteration and mineral maps (Arribas et al., 1995) were the data used in this research.

The utilized ASTER imagery consisted of Level 2 surface reflectance VNIR, and crosstalk corrected SWIR surface reflectance, acquired in 2004 over the study area. The projection is UTM zone 30 and WGS-84 datum. The WV3 were two scenes (surface reflectance) acquired in May and September 2017. It is the same projection and datum with ASTER. The WV3 data was processed to surface reflectance by Digital Globe Inc. using in situ atmospheric bands. HyMAP data (16-bit radiometric quantization) were acquired on 18 May 2004 by the German Aerospace Center (DLR) and processed to reflectance-at-surface values at a 4 m spatial sampling interval. This included geometric correction with PARGE (ReSe Applications Schläpfer, Zürich, Switzerland) and a 5m interval Digital Elevation Model (DEM), followed by an atmospheric correction with the ATCOR 4 (Atmospheric CORrection) software (ReSe Applications Schläpfer, Zürich, Switzerland). Initially in UTM zone 30 projection and European 1950 datum and for this research the datum was transformed to WGS-84, similar to ASTER and WV-3.

The VNIR and SWIR of ASTER and WV-3 were layered stacked and resampled to their respective higher resolutions. While HyMAP data were spectrally convolved to the lower resolutions of both ASTER and

WV-3 bands using spectral response functions of each sensor. The status of the datasets used in this research is summarized in table 2.1. The ASTER and the two scenes of WV-3 all differ in their nadir position, sun elevation, azimuth and viewing angles (Table 2.2). The sensors' bands wavelength ranges vary at some portions of the EMS. Table 2.3 shows the sensors bands with corresponding wavelength.

Table 2.1 Datasets used and compared in this study

Image	**Original**	**Processing carried out**	**Status used**
May WV-3	8 VNIR @ 1.2m 8 SWIR @ 7.5m	Layer stacked using nearest neighbour resampling @ 1.2m pixel.	16 bands @ 1.2m pixel
Sept WV-3	8 VNIR @ 1.2m 8 SWIR @ 7.5m	Layer stacked using nearest neighbour resampling @ 1.2m pixel.	16 bands @ 1.2m pixel
ASTER	3 VNIR @ 15m 6 SWIR @ 30m	Layer stacked VNIR-SWIR @ 15m	9 bands @ 15m pixel
HyMAP	126 bands @ 4m	2 Strips mosaicked Subsetted to WV-3 size Co-registered with WV-3	126 bands @ 4m pixel
HyMAP @ WV-3	16 VNIR-SWIR @ 4m	Spectrally resampled to WV-3	16 bands @ 4m pixel
HyMAP @ ASTER	9 VNIR-SWIR @ 4m	Spectrally resampled to ASTER resolution	9 bands @ 4m pixel

Table 2.2 Sensor's Nadir position, sun angle, azimuth and viewing angle

Sensor	Nadir line	Sun elevation	Azimuth	Viewing angle	Ground sampling distance
ASTER (6/5/2004)	10.24°	66.3°	143.3°	VNIR 8.59°	-
				SWIR 8.59°	-
WV-3 (20/5/2017)	18.2°	71.8°	212.6°	212.6°	0.34m
WV-3 (9/9/2017)	25.5°	56.7°	99.7°	99.7°	0.37m

Table 2.3 Sensors wavelength with corresponding bands

Central Wavelength (μm)	ASTER	WV-3	HyMAP@ASTER	HyMAP@WV-3
0.425	N/A	VNIR1	N/A	VNIR1
0.478	N/A	VNIR2	N/A	VNIR2
0.546	1	VNIR3	1	VNIR3
0.608	N/A	VNIR4	N/A	VNIR4
0.659	2	VNIR5	2	VNIR5
0.724	N/A	VNIR6	N/A	VNIR6
0.833	3	VNIR7	3	VNIR7
0.949	N/A	VNIR8	N/A	VNIR8
1.210	N/A	SWIR1	N/A	SWIR1
1.570	N/A	SWIR2	N/A	SWIR2
1.660	4	SWIR3	4	SWIR3
1.730	N/A	SWIR4	N/A	SWIR4
2.165	5	SWIR5	5	SWIR5
2.205	6	SWIR6	6	SWIR6
2.260	7	SWIR7	7	SWIR7
2.330	8	SWIR8	8	SWIR8
2.398	9	N/A	9	N/A

Note: N/A means not applicable

3. METHODOLOGY

3.1. General overview

The procedure of the research is summarized in figure3.1.

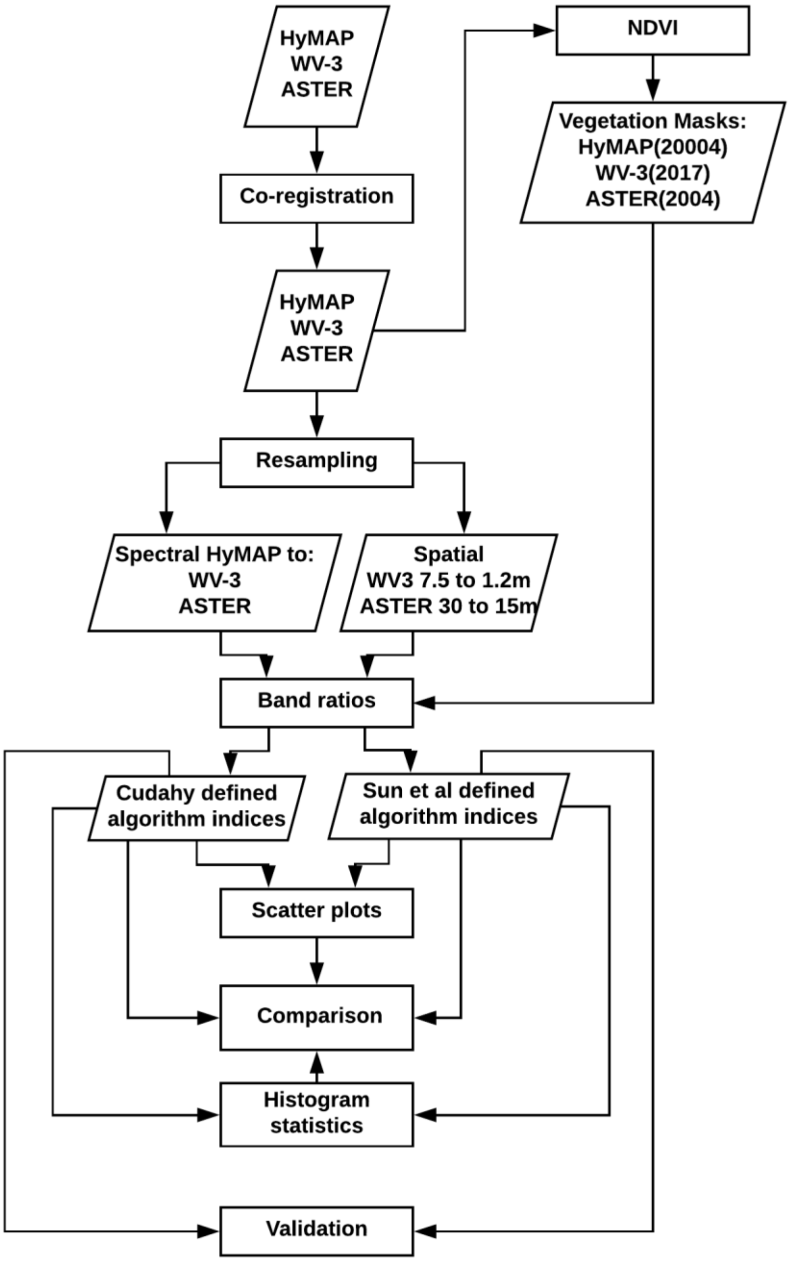

Figure 3.1 Flow chart of the research methodology

3.2. Pre-processing

The pre-processing of the images involved spatial subsetting, co-registration, vegetation analysis and resampling, masking then image comparison followed.

The images (Table 2.1) were put to the same projection, scaling and wavelength unit. HyMAP was transformed from European 1950 Datum system to WGS84, the projection of WV-3 and ASTER. Similarly, all the images reflectance values were scaled to 0-1 range, and the data types were changed from integer to floating point to keep their dynamic range. The wavelength unit of the images were all converted to micro meter (µm) for uniformity. The geographical extents of the images were different, in order to have them on to the same extents, HyMAP and ASTER were subsetted to the WV-3 size.

Furthermore, the part of the Mediterranean Sea captured in the images (Figure 4.1) was masked using elevation model (LiDAR). Surface materials (water in addition to the sea, buildings, vegetation) which are not of interest within the study area were masked. They were masked to avoid interference with the targeted AlOH, FeOH, MgOH, Kaolinite, Jarosite and Siderite mineral indices during image segmentation.

3.2.1. Image registration

Three primary images of ASTER, WV-3 and HyMAP were co-registered. The registrations were performed to have the images fit spatially, and their corresponding pixels cover as close as possible the same ground surface of the study area. The registration involved choice and collection of ground control points(GCP), feature matching of the GCPs between based and warp images, and image resampling and transformation. This was done with the consideration of geometric and radiometric deformations(Zitová & Flusser, 2003). A polynomial of order 1 transformation was chosen in order to have an optimal fitting between the images (Richards, 2013).

Selection of the GCPs was feature-based. Prominent and detectable features, road intersections, sharp bends were used as the GCPs. A total of sixty (60) ground control points(GCP) were used. The features were collected from the edges and within the body of the image (Appendix IV). Using a sufficient number of GCPs minimize the unnecessary influence on the estimated polynomial coefficients by any control points that contain significant positional errors on either image(Richards, 2013).

Finally, the 1.2m pixel size of WV-3 VNIR was resampled to the 4m pixel size of HyMAP and 15m of ASTER. The resampled WV-3 was then registered with respective images using the 60 GCPs, taking the WV-3 image as a base and the HyMAP and ASTER as warped images.

3.2.2. Vegetation analysis

A Normalized Difference Vegetation Index (NDVI) was calculated for the three images. Bands 2 & 3 of ASTER, 5 & 7 of WV-3, and 17 & 26 of HyMAP were used as Red and NIR bands respectively (Figure4.2). A linear stretch was used for all the images. By interactively adjusting the stretch values and visual inspection of the images and spectra, a threshold value of 0-0.4 was determined. This was applied to the NDVI images of WV-3, ASTER and HyMAP. In addition, the results were further compared with the weather history recorded by two weather stations Almeria, Carboneras, at the time of acquisitions of the images, (https://www.wunderground.com/history/airport/LEAM/2017/10/6/MonthlyHistory.html?&reqdb.zip=&reqdb.magic=&reqdb.wmo=). To suppress the influence of the vegetation in the area, pixels with negative NDVI value or greater than the applied threshold value (0.0-0.4) in the images were masked.

3.2.3. Resampling

To deal with the temporal difference between ASTER and WV-3 images and only have spectral/spatial differences of the sensors to work on, spectral resampling was carried out. HyMAP at 4m spatial resolution and with 126 bands, was used to simulate the spectral resolutions of the two others. The spectral response function (Figure3.2) of WV-3(Digital Globe) and the ASTER in-built response function in ENVI were used for WV-3 and ASTER respectively. The latest WV-3 spectral response available from DigitalGlobe (https://www.digitalglobe.com/resources/technical-information) was used as the in-built resampling filter function for WV-3, as ENVI has only four bands in the VNIR (380-1040) and does not match the band definition and wavelength range of WV-3. The WV-3 and ASTER both have different spatial resolutions in their VNIR and SWIR (1.2m and 7.5m, and 15m and 30m respectively). To have a combined VNIR and SWIR (9 &16) bands of ASTER and WV-3 images respectively, the two regions for each sensor were layer stacked using ENVI software. Then they were spatially resampled (using nearest neighbor transformation) to their higher resolutions of 1.2m and 15m respectively (Table2.1). The resampling to higher resolutions was preferred so as not to lose pixel information but, only splitting the larger pixels to fit into the array of the small pixels.

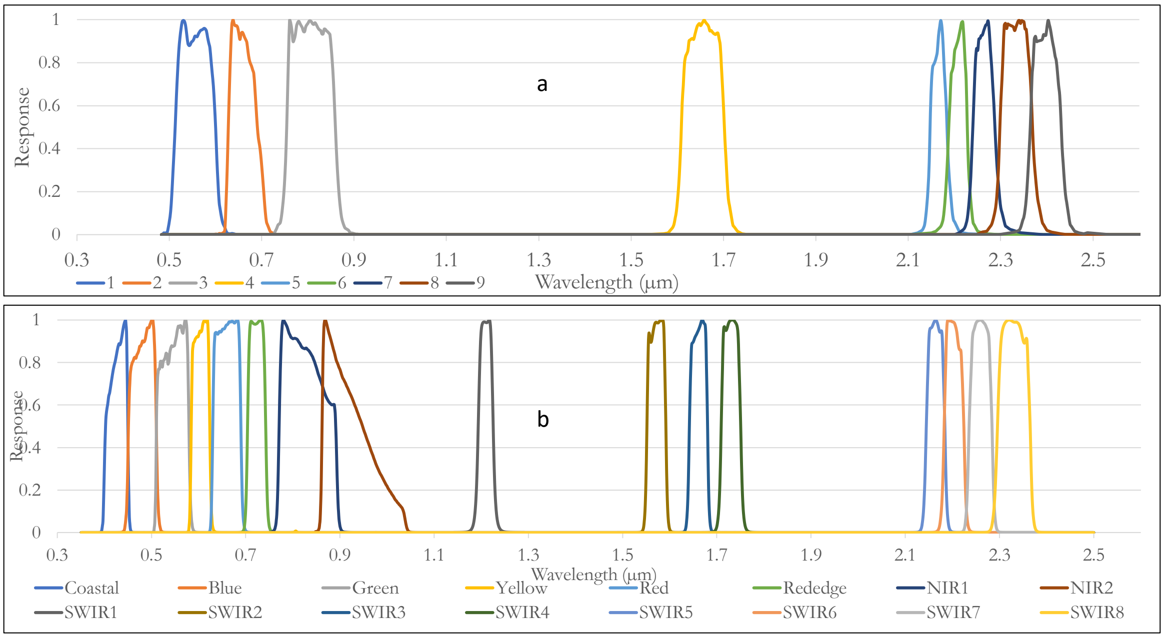

Figure 3.2 Spectral response functions for ASTER & WV-3 (a) Spectral response function of the 9 bands of ASTER, in-build in ENVI classic software. (b) The latest spectral response function of the 16 bands of WV-3 (https://www.digitalglobe.com/resources/technical-information).

3.3. Image comparison

WV-3 and ASTER capabilities for mineral mapping in hydrothermal alteration system were compared. The comparison was principally based on band ratios, using two different algorithms defined by (Cudahy, 2012; Sun et al., 2016). The WV-3, ASTER, and the HyMAP products used as the control were all classified twice with the two different sets of algorithms and the results were compared. The resulting images were further compared using scatter plot visualization and statistics of the index histograms.

3.3.1. Band ratios

A knowledge based approach (band ratios) using absorption modelling (Asadzadeh & de Souza Filho, 2016) was used to classify and compare the images. It is based on the discrete characteristics of the absorption features of the images materials(van der Meer, 2004; Clark, 1999; Mustard & Sunshine, 1999). Band ratios are a common approach in image processing, where there are differences in reflectance between absorptions and their shoulders (Asadzadeh & de Souza Filho, 2016; Langford, 2015; Inzana et al., 2003). It gives an estimation of the absorption band depth (Asadzadeh & de Souza Filho, 2016). In addition to the simplicity of the technique, it is insensitive to illumination and topography effects, suppresses variations in reflectance albedo, and differences related to grain size (Langford, 2015).

Two algorithms; one defined by Cudahy (2012) and the other by Sun et al., (2016) initially designed for ASTER and WV-3 respectively, were used. This led to two categories of comparison: Firstly, each algorithm was applied to the sensor initially it was defined for. Secondly, the algorithm specific for ASTER was applied on WV-3 and *vice-versa*. Table 3.1 and 3.2 show the corresponding bands for each of the indices in the different images used. The resulting index map on ASTER were compared with the index map from WV-3. In all cases, HyMAP imagery was spectrally resampled to ASTER and WV-3 and processed by the same algorithms in order to be used as a control.

Six indices (kaolinite, AlOH, MgOH, ferrous iron in MgOH/carbonate, jarosite, siderite) from the two algorithms were chosen to be used in comparing the images. The choice was based on what wavelength bands the sensors have in common, and the consideration of the significance of the mineral groups in the interpretation of host rock or hydrothermal alterations. However, the sensors differ in their instrumental designs. WV-3 has more bands in the VNIR than ASTER and one less in the SWIR (Figure 1.1). ASTER does not have the corresponding VNIR6 (0.704-0.745), VNIR8(0.860-1.040) and SWIR1(1.195-1.225) of WV-3. Similarly, WV-3 does not have the corresponding SWIR9(2.360-2.430) of ASTER (Table 2.3). Because of the band's differences, MgOH index defined by Cudahy was not applied to WV-3 images. Likewise, FeOH, jarosite and siderite indices defined by Sun et al were not applied to the ASTER image (Table 3.1 & 3.2). Furthermore, ASTER has limited (3) bands in the VNIR. It does not have the corresponding VNIR6 and 8 of WV-3, therefore, the Sun's defined jarosite and siderite indices were not applied to the ASTER image. Instead, FeOH group content and ferrous iron content in MgOH/carbonate definitions by Cudahy were used for the possible highlight of jarosite and siderite groups in ASTER respectively. Also, ASTER does not have the corresponding SWIR1 of WV-3, and therefore, the Sun's FeOH defined index was not applied to ASTER scene. On the other hand, the WV-3 does not have the corresponding ASTER band 9. Hence, the MgOH Cudahy defined index was not applied to the WV-3 scene.

The Cudahy algorithm was initially used for regional mapping in Australia, and the default stretches and thresholds were set based on the ASTER experience over Australia (Cudahy, 2012). The default thresholds for the Cudahy algorithm were applied in this work as well. For the Sun et al, linear stretch was applied, and the interactive histogram in ENVI and the spectral profiling was used to determine the threshold.

Table 3.1 Cudahy defined algorithm for ASTER (Cudahy, 2012)

Indices	**Original definition**	**Bands used**				
		ASTER	MayWV-3	SeptWV-3	HyMAP @ ASTER	HyMAP@ WV-3
Al-OH	[B5+B7]/B6	√	[SWIR5+SWIR]/SWIR6	[SWIR5+SWIR7]/ SWIR6	√	[SWIR5+SWIR7]/SWIR6
Mg-OH	[B6+B9]/ [B7+B8]	√	N/A	N/A	√	N/A
Fe-OH	[B6+B8]/B7	√	[SWIR6+SWIR8]/SWIR7	[SWIR6+SWIR8]/ SWIR7	√	[SWIR6+SWIR8]/SWIR7
Kaolinite	B6/B5	√	SWIR6/SWIR5	SWIR6/SWIR5	√	SWIR6/SWIR5
Ferric oxide	B4/B3	√	SWIR3/VNIR7	SWIR3/VNIR7	√	SWIR3/VNIR7
Ferrous iron	B5/B4	√	SWIR5/SWIR3	SWIR5/SWIR3	√	SWIR5/SWIR3
Ferrous iron content in Mg-OH/ Carbonate	B5/B4	√	SWIR5/SWIR3	SWIR5/SWIR3	√	SWIR5/SWIR3

NB: The original definitions were used for the HyMAP spectrally resampled to ASTER.
N/A means not applicable

Table 3.2 Sun et al defined algorithm for WV-3 (Sun et al., 2016)

Indices	**Original definition**	**Band used**					
		May WV3	Sept WV3	ASTER	HyMAP	HyMAP@WV3	HyMAP@ASTER
Al-OH	[SWIR3/SWIR6]*[SWIR7/SWIR8]	√	√	[B4/B6]*[B7/B8]	[B80/B108]*[B111/B115]	[B11/B14]*[B15/B16]	[B4/B6]*[B7/B8]
Mg-OH	[SWIR6/SWIR8]*[SWIR3/SWIR8]	√	√	[B6/B8]*[B4/B8]	[B108/B115]*[B80/B115]	[B14/B16]*[B11/B16]	[B6/B8]*[B4/B8]
Fe-OH	[SWIR3/SWIR7]*[SWIR3/SWIR1]	√	√	N/A	[B80/B111]*[B80/B52]	[B11/B15]*[B11/B9]	N/A
Carbonate	[SWIR6/SWIR8]*[SWIR3/SWIR8]	√	√	[B4/B8]	[B108/B115]*[B80/B115]	[B14/B16]*[B11/B16]	[B6/B8]*[B4/B8]
Kaolinite	[SWIR3/SWIR5]*[SWIR8/SWIR6]	√	√	[B4/B5]*[B8/B6]	[B80/B106]*[B115/B108]	[B11/B13]*[B16/B14]	[B4/B5]*[B8/B6]
Jarosite	[VNIR6/SWIR7]	√	√	N/A	[B19/B111]	[B6/B15]	N/A
Siderite	[VNIR8/SWIR1]	√	√	N/A	[B29/B52]	[B8/B9]	N/A

N/A means not applicable

3.3.2. Scatter plots and statistics

A scatter plot is a matrix composed of 2-D plots that give a visual measure of correlation between two variables. Both the vegetation index (NDVI) and the mineral indices (band ratios) were analysed with the scatter plots. The vegetation cover differences in the images were examined by comparing the images NDVIs: May 2017 WV-3 *versus* September 2017 WV-3; May 2017 WV-3 *versus* May 2004 ASTER and September 2017 WV-3 *versus* May 2004 ASTER. For the band ratios comparison, the indices ratio maps: May WV-3 *versus* September WV-3; May WV-3 *versus ASTER*; and September WV-3 *versus* ASTER were compared. HyMAP spectrally resampled to WV-3 *versus* HyMAP spectrally resampled to ASTER were also compared as a control for the compositional ratio product.

Based on the values representing the indices, regions of interest were defined within the plots clustering associated pixels (Jourdan et al., 2007). This is to highlight compositions and spatial locations of the index anomalies. Region of interests (ROI) were delineated for different data point clouds at the higher values (representing the index product) and the lower values (not representative of the index). A threshold segmentation technique based on the pixels intensity (Oak, 2016), using histogram approach (Saleh Al-Amri et al., 2010) was used in separating the peaks. The technique is suitable for real time application (Oak, 2016), and when compared to other segmentation techniques it has best performance, good segmentation effect and low complexity (Dubey et al., 2016; Karungan & Sujatha, 2017). The position of the absorption features relative to the shoulder bands were also considered in determining the threshold values representative of the indices (Hecker et al., 2007).

However, in thresholding, sometimes the pixels are not contiguous and may include extraneous pixels that are not part of the class of interest or simply miss isolated pixels that belong to the class of interest. To deal with this and to support the determination of the threshold values, the ROIs were exported and overlaid on the respective ratio maps to verify their distribution in the expected locations. Furthermore, spectral similarity between the ROI mean spectra and the ASD field spectra were compared to have confidence that the spectra represent the mineral identified in the field. The ASD spectra were collected in September 2017 by ITC personnel during the reference measurements in the WV-3 data acquisition. The spectra were further compared and verified with USGS resampled ASTER and WV-3 spectral libraries.

The relationship that exists between the images in mapping the indices products were further described with the correlation coefficients of the products. Mean values of the indices were used to quantify the differences between the images and the variance there after were determined.

3.4. Validation

The results of the ratios indices were compared with the published alteration map by Arribas (Arribas, 1995) and the geology and mineral maps of the area (Arribas, 1993). HyMAP was used as a control during the processing of the WV-3 and ASTER images.

4. RESULTS

The chapter presents the results of the NDVI, band ratios, scatter plots and statistics used for the image processing and comparison in this research.

4.1. NDVI

Figure 4.1 shows a false - colour infrared (CIR) of the images used in this research. They were acquired over the study area at different seasons. ASTER 6th May 2004, HyMAP on the 18th May 2004, and the two scenes of WV-3 on the 20th May and 9th September 2017 respectively.

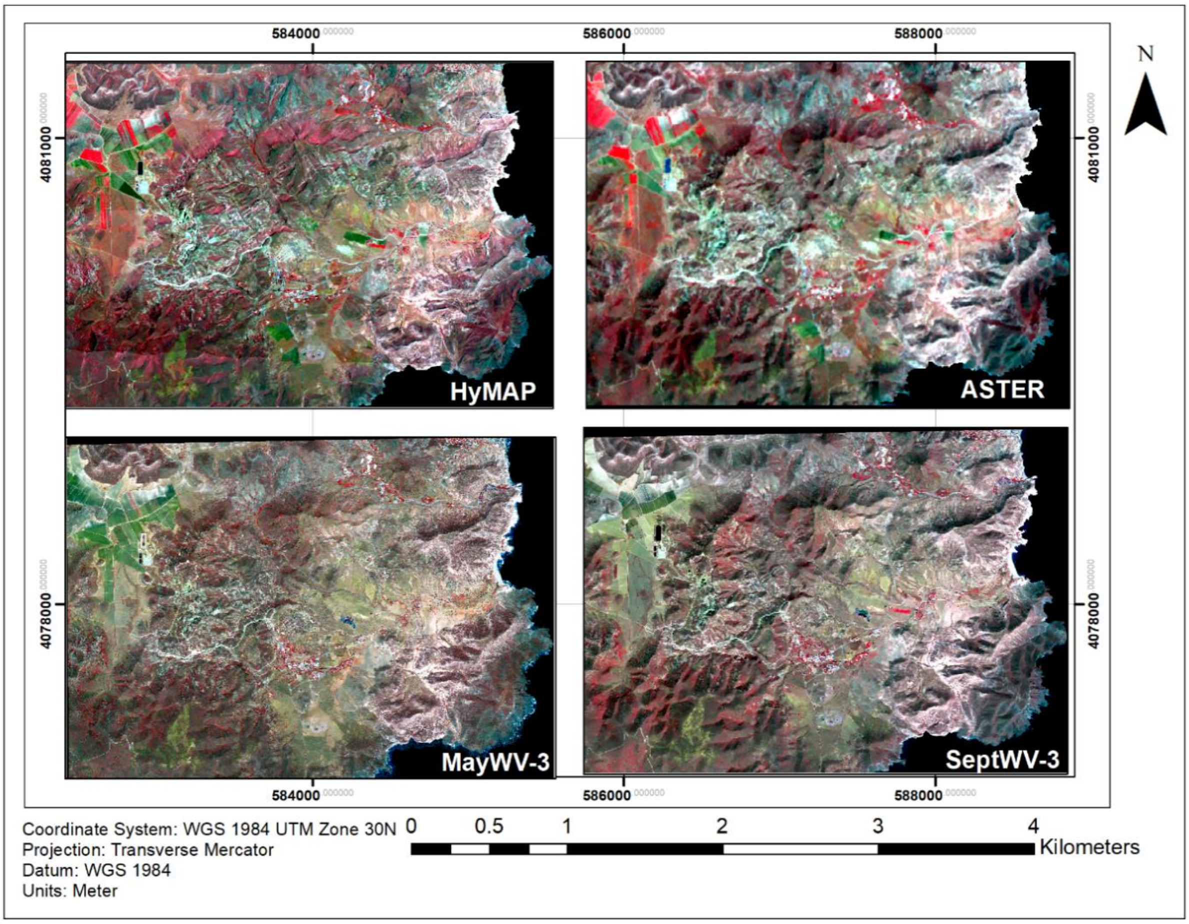

Figure 4.1 False Colour Infrared (CIR) view of the dataset used in this research. HyMAP which was used as a control, ASTER which was compared to the two scenes of WV-3.

NDVI was calculated for the four images, and the results are shown in Figure 4.2. This was used with a consistent threshold of 0.4 to mask vegetation in the study area. In the 2004 acquisitions, HyMAP scene with NDVI mean value of 0.353 has more vegetation cover than ASTER scene with NDVI mean value of 0.277. In the 2017 acquisitions, the images slightly differ, in some parts, the May has more vegetation, and likewise in some part, the September image has more vegetation. The May acquisition has NDVI mean value of 0.224 while the September acquisition with a mean value of 0.223. This shows slightly more vegetated in May than in September acquisition. Comparing the 2017 WV-3 with 2004 ASTER acquisitions by the mean NDVI values, the result shows that the area is less vegetated in 2017.

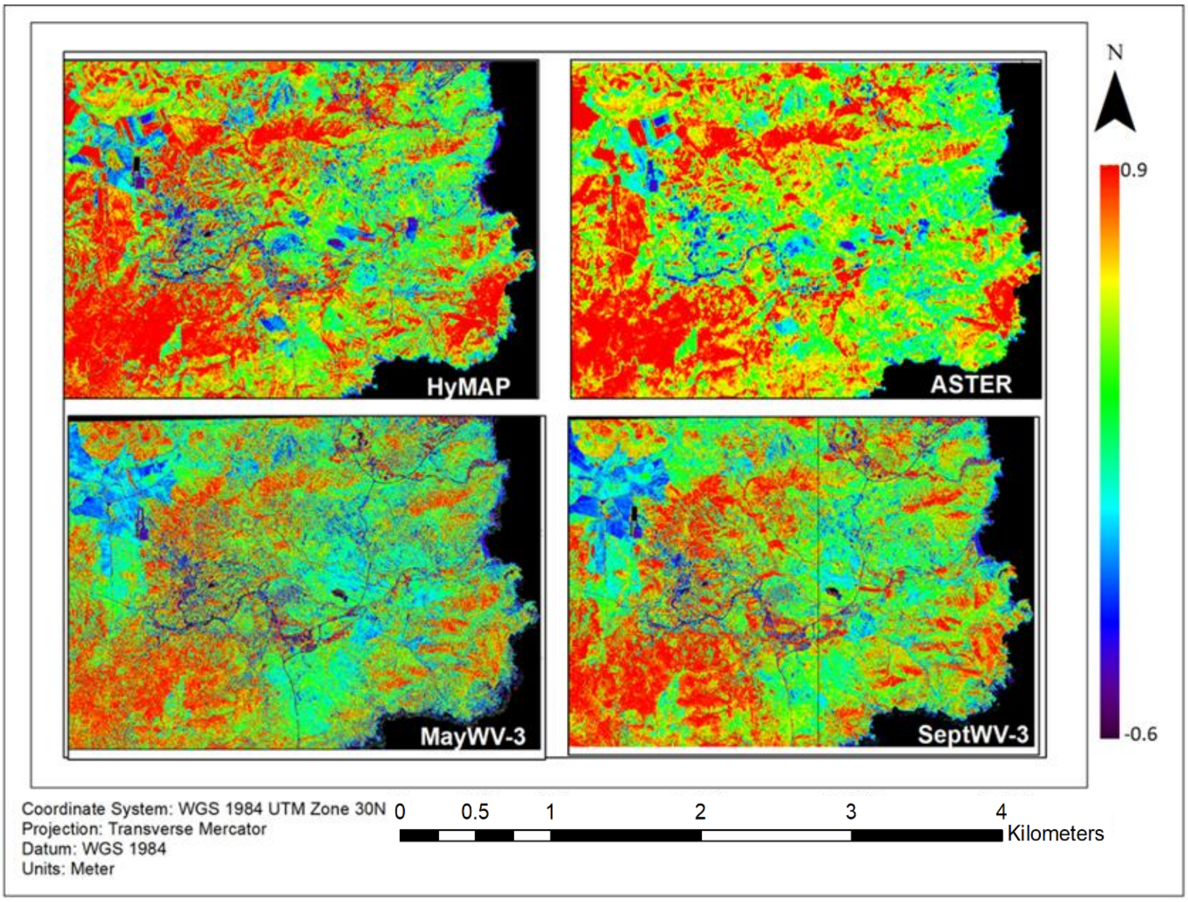

Figure 4.2 NDVI results for 2004 (HyMAP, ASTER) and 2017 (WV-3) acquisitions. It shows that the area is less vegetated in 2017 compared to 2004.

To further analyse the greeness of the area, the NDVI results were compared using scatter plots as shown in figure 4.3. It shows that the vegetation cover in May and September 2017 were moderately correlated (r: 0.49), although some population peaks are not on 1-1 relationship. In (b) the population clouds are more to HyMAP than in ASTER which shows more green in the HyMAP. The correlation coefficient value (0.44) indicated a moderate correlation of vegetation cover between the HyMAP and ASTER images. Plots c and d compare ASTER to the two scenes of WV-3. The plots show very poor correlation (r: 0.24 and 0.18) which revealed clear differences between 2004 and 2017 in vegetation cover. It shows more vegetation cover in 2004 than in 2017.

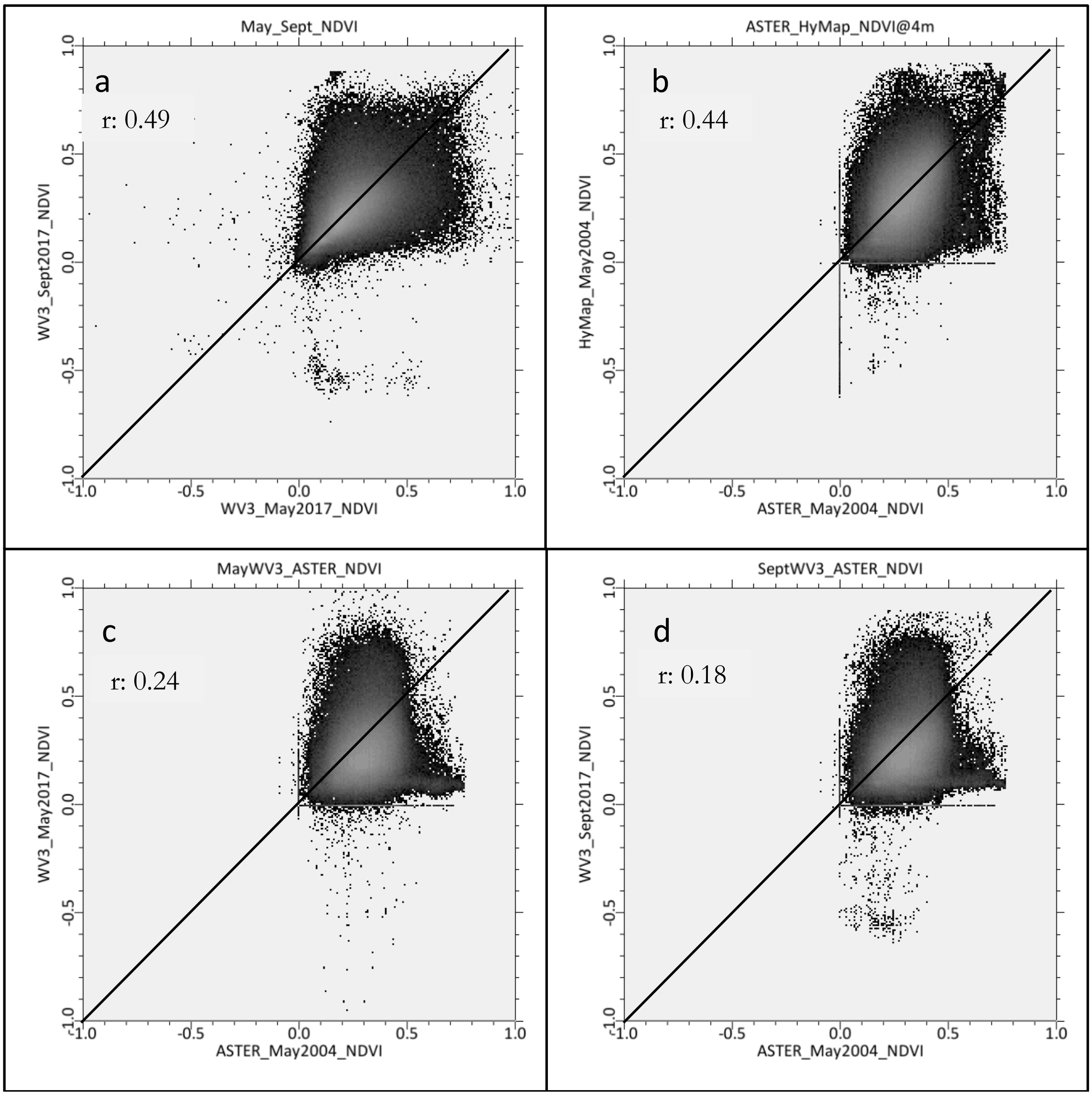

Figure 4.3 Scatter plots of NDVI results with their respective correlation coefficient. (a) Comparison between May 2017 & September 2017 scenes of WV-3, it shows moderate relationship. (b) The relationship between HyMAP 2004 & ASTER 2004, it shows poor correlations, ASTER high values correspond with the medium to high values of HyMAP. (c) Relationship between ASTER 2004 & MayWV-3 2017, and (d) Relation between ASTER 2004 & SeptWV-3 2017. At the bottom, the comparison between ASTER and May as well as with September WV-3 images both show poor correlations as well.

4.2. Band ratios

Two different algorithms defined by Cudahy (2012) and Sun et al. (2016) were used to compare the prediction of six (AlOH, MgOH, Kaolinite, Ferrous iron, Jarosite and siderite) indices by ASTER and WV-3. The band ratios comparisons are in twofold: First is comparing the WV-3 images with ASTER, and the second compares the May and September acquisitions of WV-3 using the Sun et al algorithm. The index images are displayed on the subsequent sections 4.2.1 and 4.2.2. Respective vegetation masks were applied to all the images (ASTER, WV-3, HyMAP) before the indices.

4.2.1. Cudahy defined algorithm results

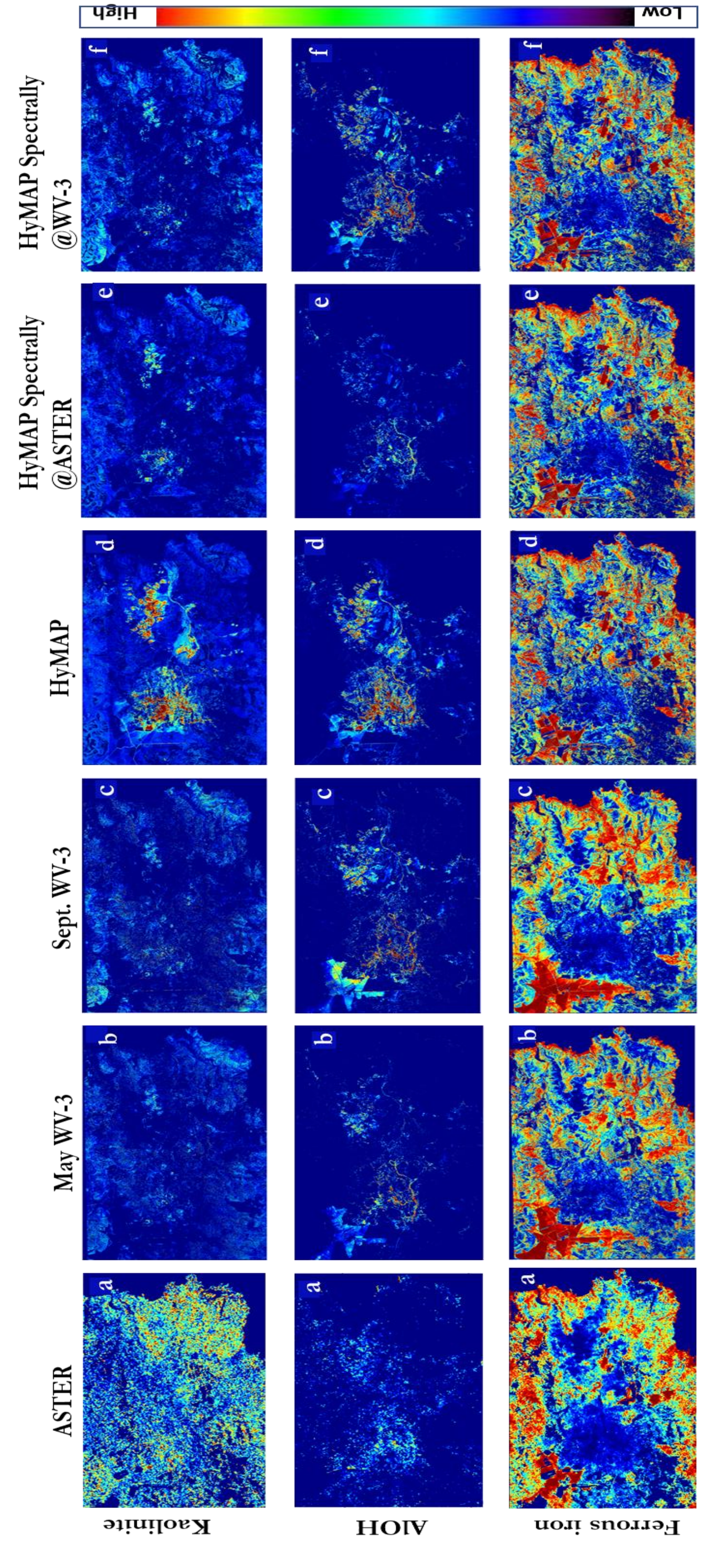

Figure 4.4 Band ratio maps for Kaolinite, AlOH and Ferrous iron using Cudahy defined algorithm, default stretches and thresholds. Red-Blue colour contrast was used. Blue indicates low to zero while red indicates high contents. For kaolinite, comparing ASTER with WV3 images, based on the spatial coverage and the colour rating, the images are described as follows: ASTER looks noisy, displays different pattern compared with the other images and the knowledge of the alteration zones in the area. In the two WV3 images, the prediction was very low. Also for AlOH using HyMAP as a control, the prediction was better in WV3 by highlighting the alteration zones than ASTER. Comparing the two WV3 images, the September acquisition predicts more than the May acquisition. For ferrous iron, the three images predict the product relatively similar. Although the WV3 images did better than ASTER and HyMAP. Between the WV3 images, the September predict little more than the May acquisition.

4.2.2. Sun et al defined algorithm results

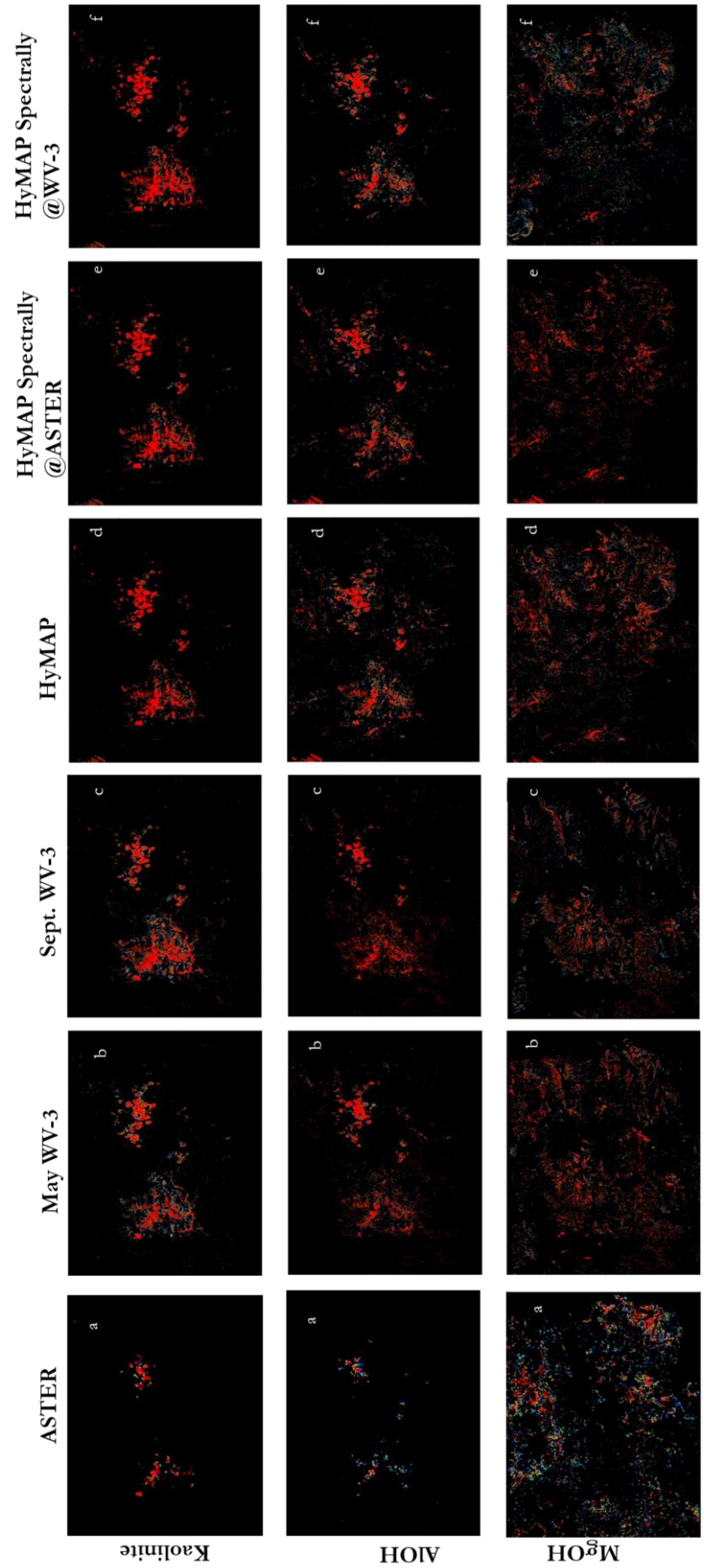

Figure 4.5 Band ratio maps from the six images for three indices using the Sun et al algorithm. The ratio maps of kaolinite and alunite produced with ASTER show very low discrimination of the indices when compared to WV-3. It also shows the ASTER image inability to pick up the small lower alunite as seen in WV3 and HyMAP. The WV3 and HyMAP show very similar prediction of the three indices. They highlighted more clearly the known alteration areas. For MgOH, all the six images show very similar discrimination of the product. In the WV-3 images, the HyMAP and WV-3 simulated HyMAP, the predictions for the three indices were more pronounced than in ASTER. The mean Spectra of each of the images is on figures 4.6.4

Figures 4.6 shows the mean spectra collected from the regions highlighting the index product on each of the images (ASTER, WV-3, ASTER and WV-3 simulated HyMAP). The spectra were compared with the minerals spectra in the USGS resampled libries for true representation of the indices.

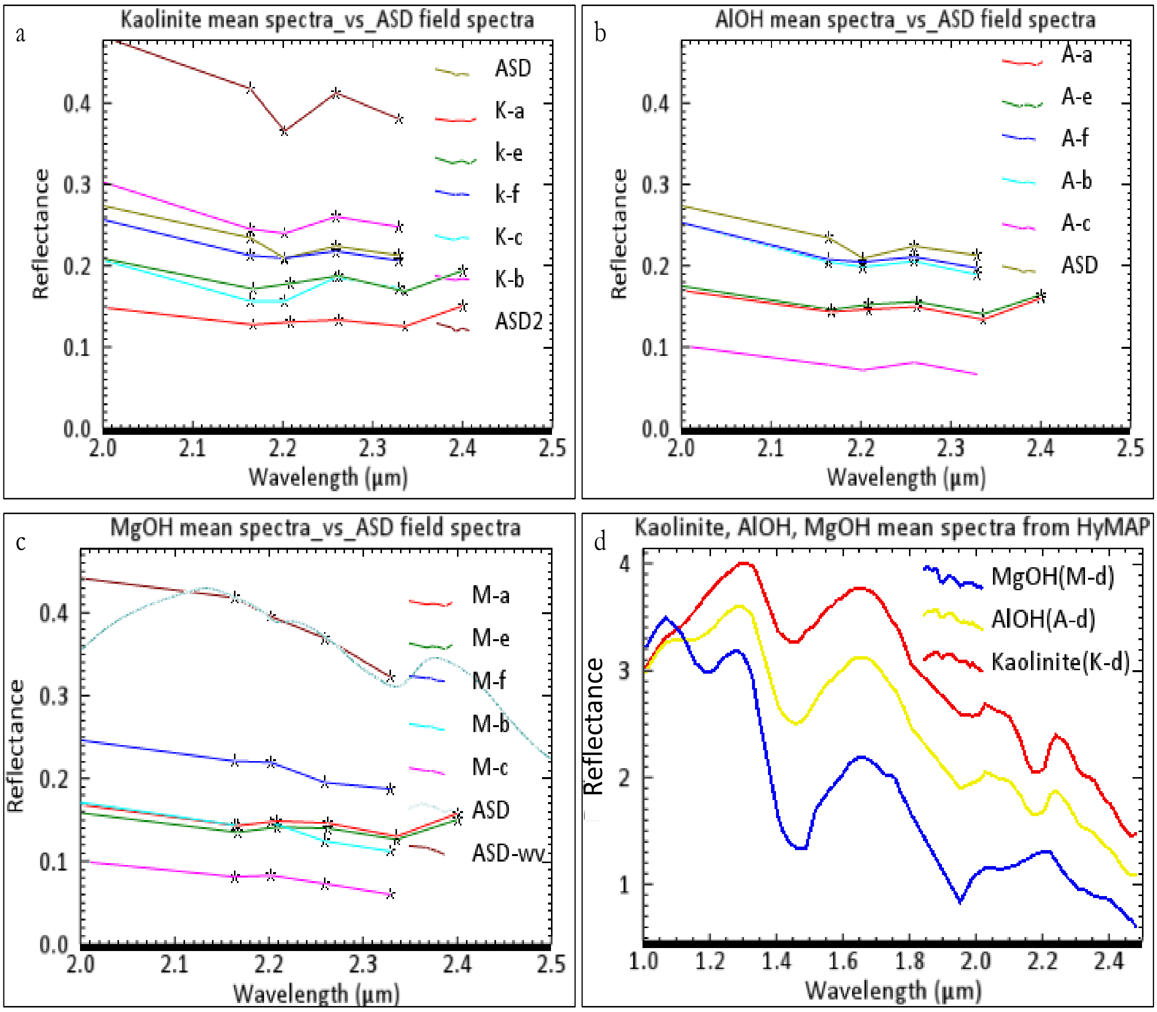

Figure 4.6 Mean spectra of the kaolinite, AlOH and MgOH indices taken from the ratio product of the five images used in the research. (a) Kaolinite index mean spectra from ASTER [k-a], MayWV-3 [k-b], SepWV-3 [k-c], simulated ASTER by HyMAP [k-e], simulated WV-3 by HyMAP [k-f] compared to ASD measurements resampled to WV-3 spectra. (b) AlOH index mean spectra from ASTER [A-a], MayWV-3 [A-b], SepWV-3 [A-c], simulated ASTER by HyMAP [A-e], simulated WV-3 by HyMAP [A-f] compared to ASD measurements resampled to WV-3 spectra. (c) MgOH index mean spectra from ASTER [M-a], MayWV-3 [M-b], SepWV-3 [M-c], simulated ASTER by HyMAP [M-e], simulated WV-3 by HyMAP [M-f] compared to ASD measurements resampled to WV-3 spectra, and (d) Kaolinite [k-d], AlOH and MgOH indices mean spectra from the ratio products of the HyMAP original image.

4.3 Scatter plots

The band indices calculated for ASTER and WV-3 were further compared using scatter plots. High values represent the population of the index in the axis while low values indicate a different anomaly. In the plots below, the red pixels cloud highlights the population of the high values of the index on the y-axis. The yellow pixels cloud highlights the population of the high values of the index on the x-axis. The blue circle highlights the populations of low values of the two indices. Where the indices have a linear relation, the data points will form a diagonal line depending on the degree of the correlation. If the comparing variables are not related, different populations cloud are formed. The comparisons are as presented below:

4.2.3. WV-3 - May and September 2017 acquisitions.

Six indices (Kaolinite, AlOH, MgOH, FeOH, Jarosite, Siderite) were calculated following table 3.2 to compare the two different WV-3 acquisitions. Plot (a) shows a high correlation between the images in discriminating kaolinite index. Pixels with a value above 2 matches with the spectra of kaolinite and their spatial distribution on the index map fall within the alteration areas. The low value pixels fall along the coast and stream channels. Plots (b-d) also show correlations between the images for the three indices (AlOH, MgOH, FeOH). Pixels with values above 2.2 match the spectra of AlOH, 2.7 matches the spectra MgOH and 2.1 matches the spectra of FeOH. In (e), pixels with values above 1.7 matches with jarosite. The plot shows poor correlation between the images. Overlaying the regions of interest on the index maps shows more jarosite in May scene than in September. Plot (f) also shows poor correlation for siderite. The May acquisition has more siderite than the September.

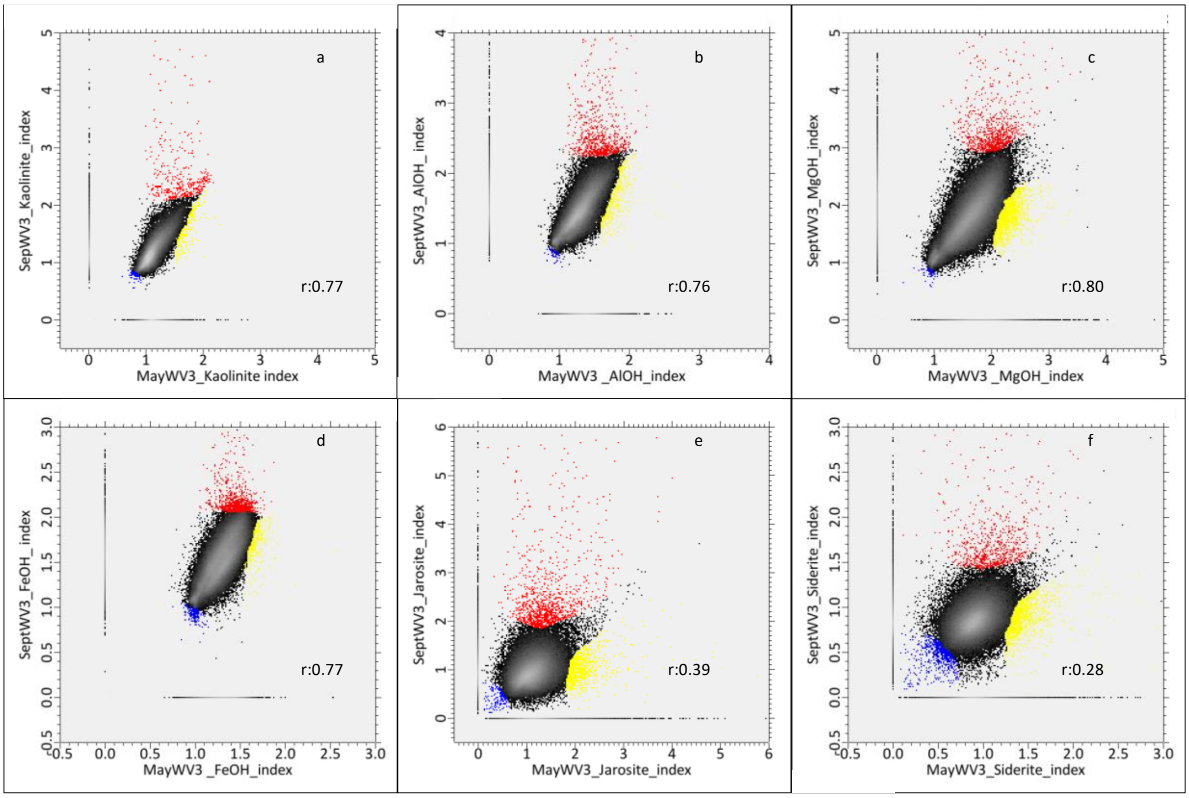

Figure 4.7 Indices comparisons between May and September acquisition of WV-3. The red colours are areas (pixels) with high values for the index on the y-axis, and the yellow colour are areas (pixels) with high values for the index on the x-axis. They indicate pixels that match with the index spectra and spatially on the ratio maps indicates areas of the alteration. The blue colour indicates pixel with low values and do not represent the index mineral.

The high and low values were exported as regions of interest and plotted onto the respective ratio image to evaluate their distribution with respect to the alteration zones. Mean spectra were collected for confirmation of the representation of the index. Figures 4.8 – 4.13 show the distribution of the high and low values in the May and September acquisitions with their respective spectra.

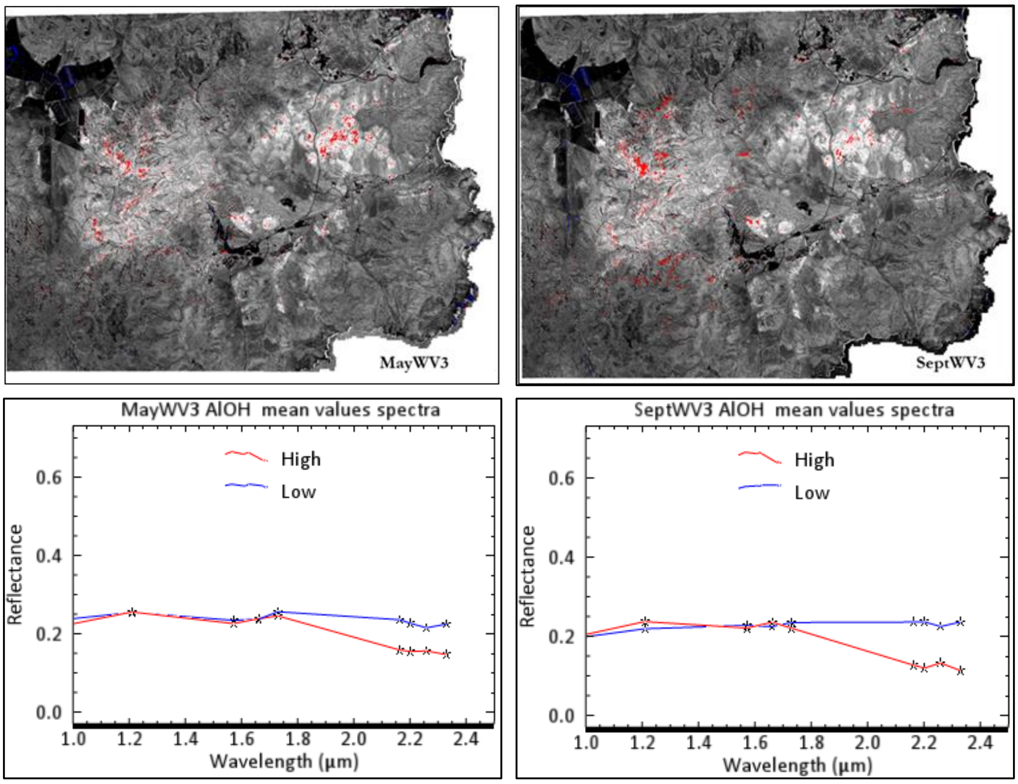

Figure 4.8 High and low pixels values for AlOH in May and September acquisition with respective mean spectra. The red spectra represent the pixels with high values, while the blue represents pixels with low values.

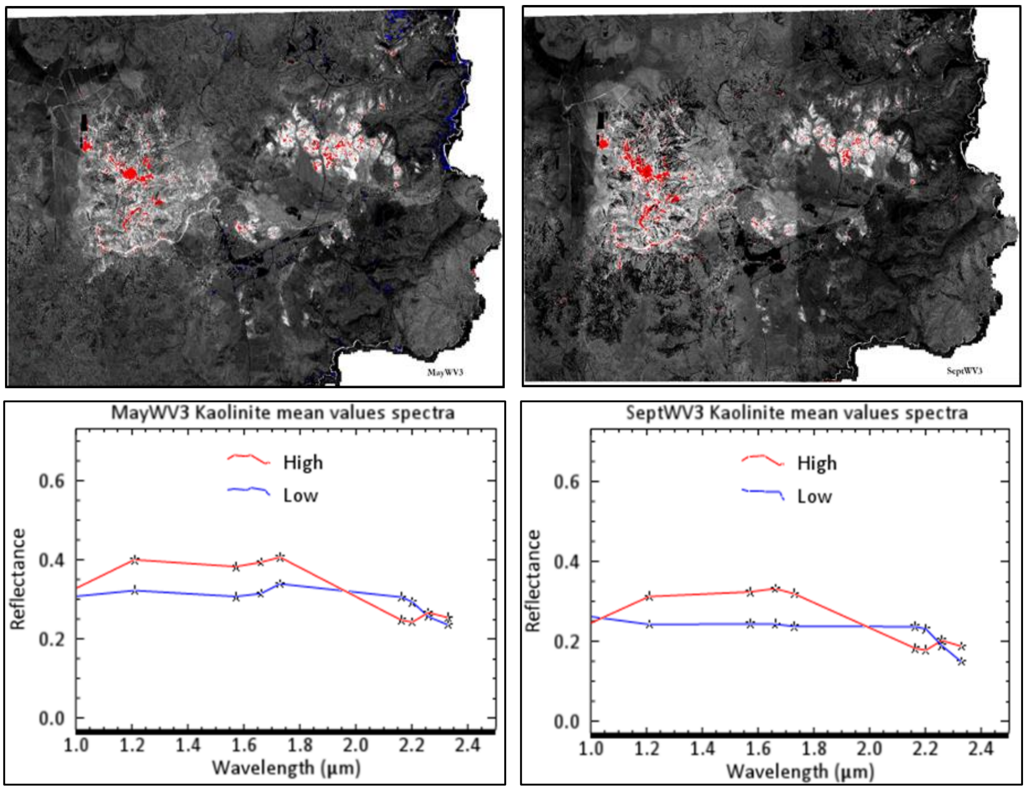

Figure 4.9 High and low pixels values for Kaolinite in May and September acquisition with respective mean spectra. The red spectra represent the pixels with high values, while the blue represents pixels with low values.

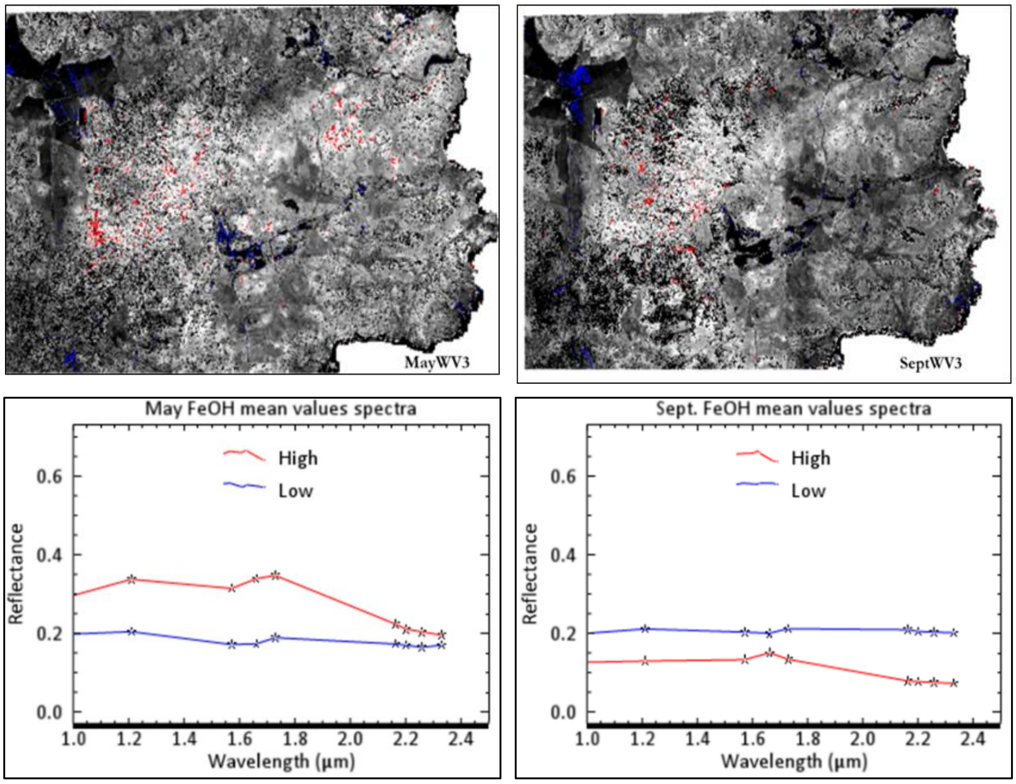

Figure 4.10 High and low pixels values for FeOH in May and September acquisition with respective mean spectra. The red spectra represent the pixels with high values, while the blue represents pixels with low values.

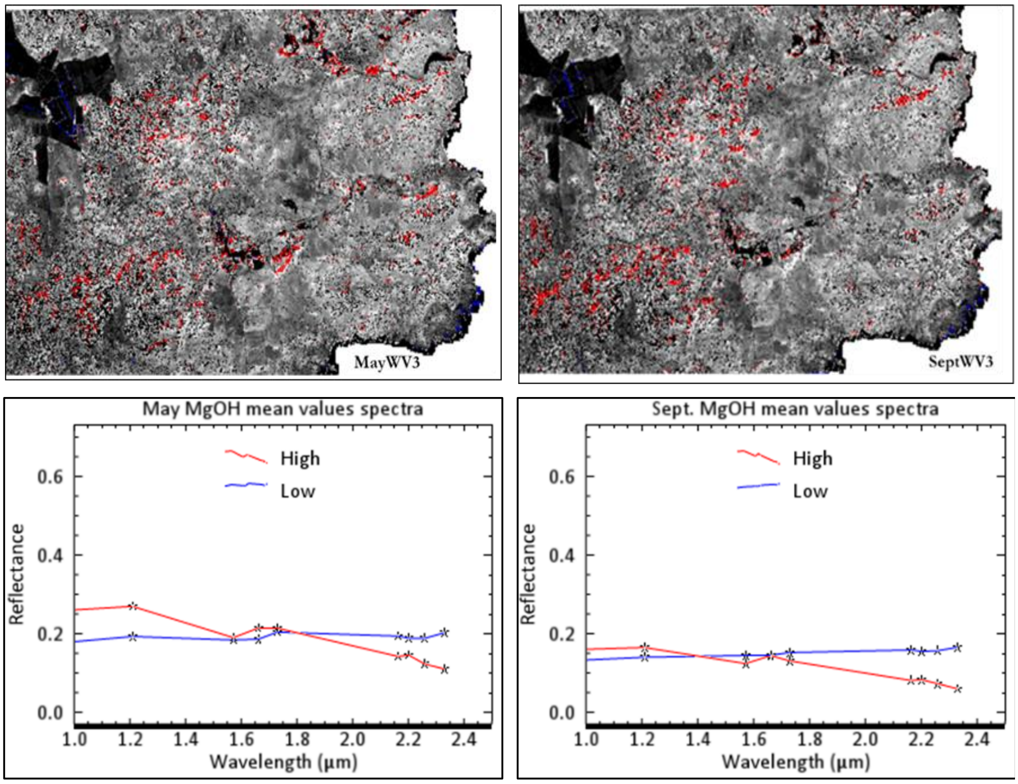

Figure 4.11 High and low pixels values for MgOH in May and September acquisition with respective mean spectra**.** The red spectra represent the pixels with high values, while the blue represents pixels with low values.

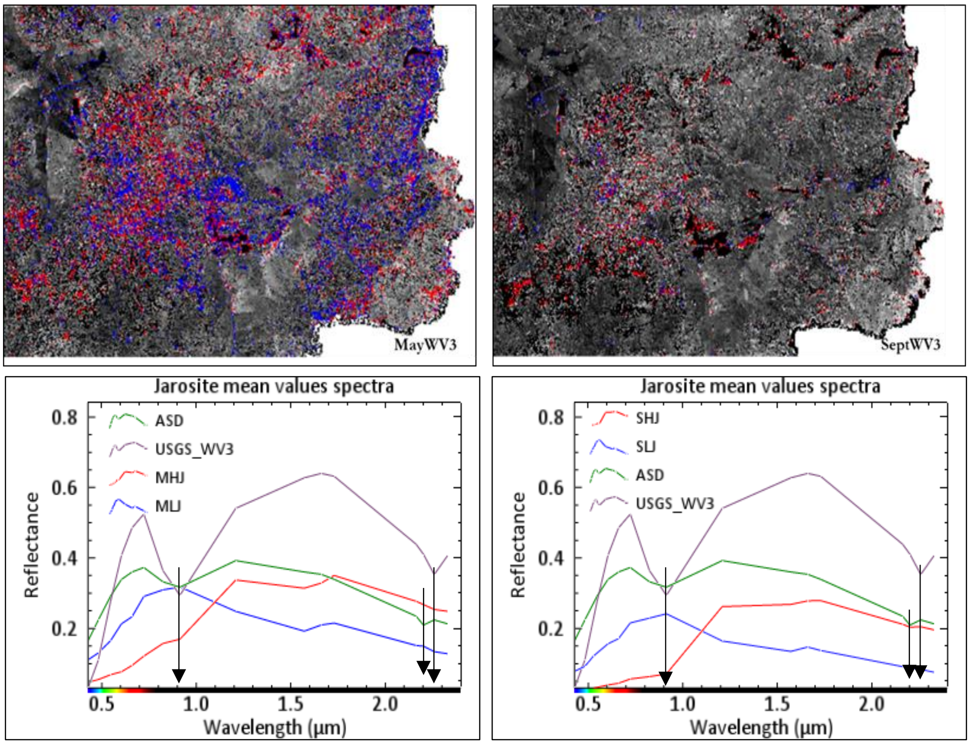

Figure 4.12 High and low pixels values for jarosite in May and September acquisition with respective mean spectra compared to ASD field spectra and USGS resampled WV-3 spectra. The red spectra represent the pixels with high values, while the blue represents pixels with low values. Green represent ASD spectra and brown represent USGS spectra. The index abundance is quite different; it is more in May than in September scene.

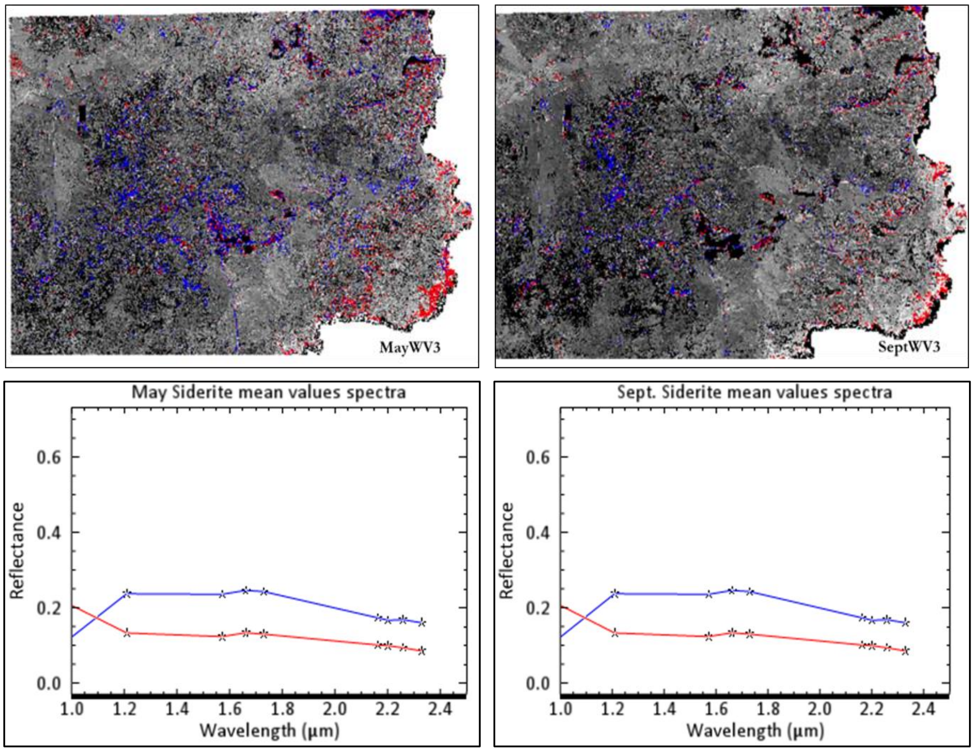

Figure 4.13 High and low pixels values for siderite in May and September acquisition with respective mean spectra. The red spectra represent the pixels with high values, while the blue represents pixels with low values.

4.2.4. ASTER versus WV-3 acquisitions using Sun et al algorithm.

ASTER image is compared with the May and September WV-3 images using the Cudahy and Sun's definitions. The indices selected for the comparison are AlOH, Kaolinite, MgOH, and ferrous iron were used. These were selected because both sensors have bands that do create the indices.

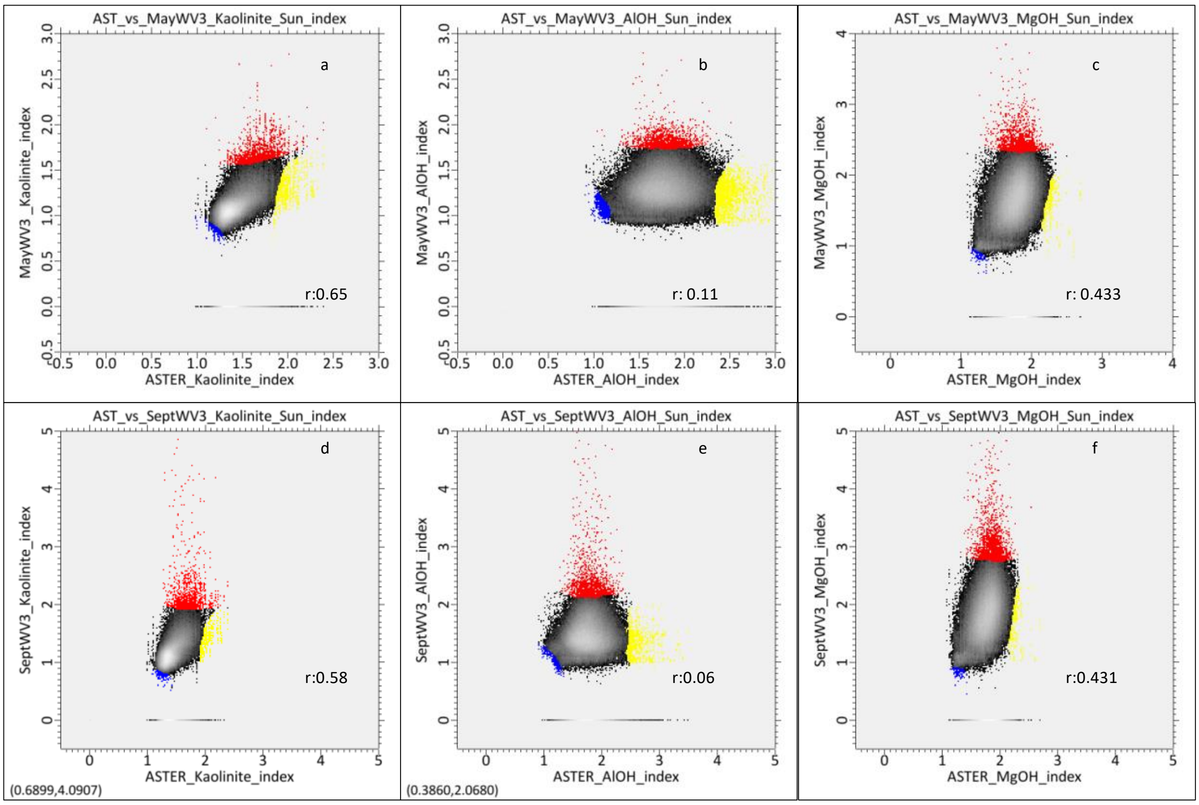

Figure 4.14 Scatter plots of ratios defined by Sun et al. The red colours are areas (pixels) with high values for the index on the y-axis and the yellow colour are areas (pixels) with high values for the index on the x-axis. They indicate pixels that match with the index spectra and spatially on the ratio maps indicates areas of the alteration. The blue colour indicates pixel with low values and do not represent the index mineral.

The plots show poor to no correlation between ASTER and WV-3. Plots a-c above display the ASTER versus May WV-3 while below (d-f) display ASTER versus September WV-3. In general, ASTER has low values compared to WV-3. In both May and September, the relationship is quite similar where ASTER high values correspond to the WV-3 low values. Except for MgOH where the ASTER high values correspond to the low to medium values of WV-3. Plotting the values spatially on the index maps matches the WV-3 high values with the known alteration areas. The ASTER high values highlight areas along the coast and some disturbed areas.

The clouds of high and low densities in the scatter plots were thresholded and exported onto the respective ratio image to see their locations on the images. Mean spectra were collected for confirmation of the representation of the index. The results are displayed in figures 4.15 – 4.17

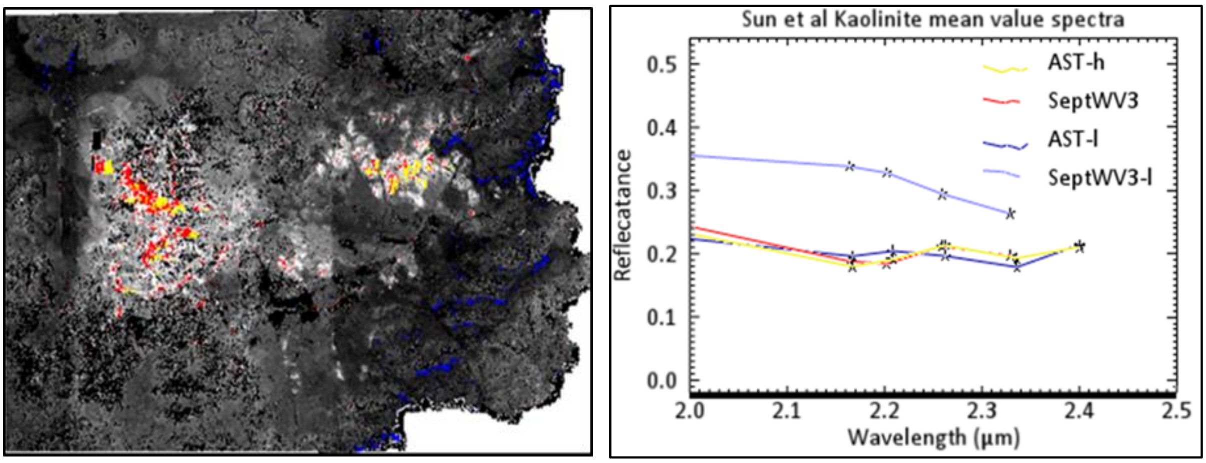

Figure 4.15 High and low pixels values for Kaolinite in ASTER and September acquisition with respective mean spectra calculated using Sun et al algorithm. The red and yellow spectra represent the pixels with high values for WV-3 and ASTER respectively. The blue represents pixels with low values. This indicates moderate correlations between ASTER and WV-3.

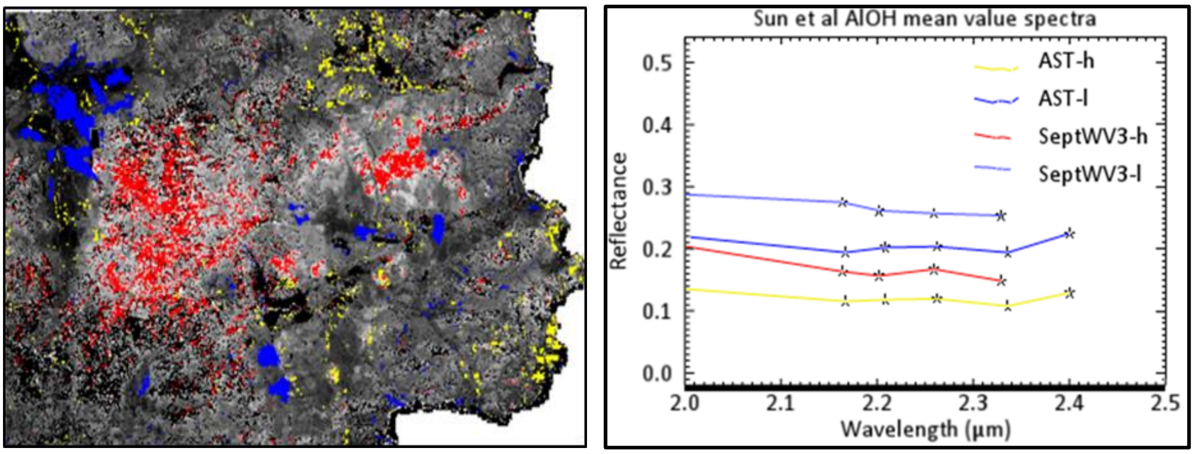

Figure 4.16 High and low pixels values for AlOH in ASTER and September acquisition with respective mean spectra calculated using Sun et al algorithm. The red and yellow spectra represent the pixels with high values for WV-3 and ASTER respectively. The blue represents pixels with low values. This indicates poor correlations between ASTER and WV-3.

.

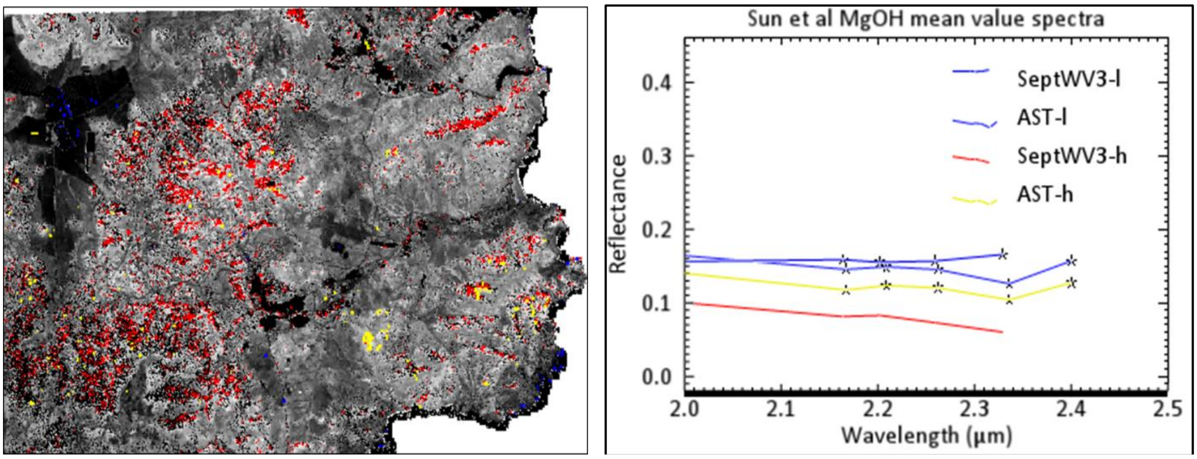

Figure 4.17 High and low pixels values for MgOH in ASTER and September acquisition with respective mean spectra calculated using Sun et al algorithm. The red and yellow spectra represent the pixels with high values for WV-3 and ASTER respectively. The blue represents pixels with low values. This indicates poor correlations between ASTER and WV-3.

4.3.3 ASTER versus WV-3 acquisitions using Cudahy algorithm.

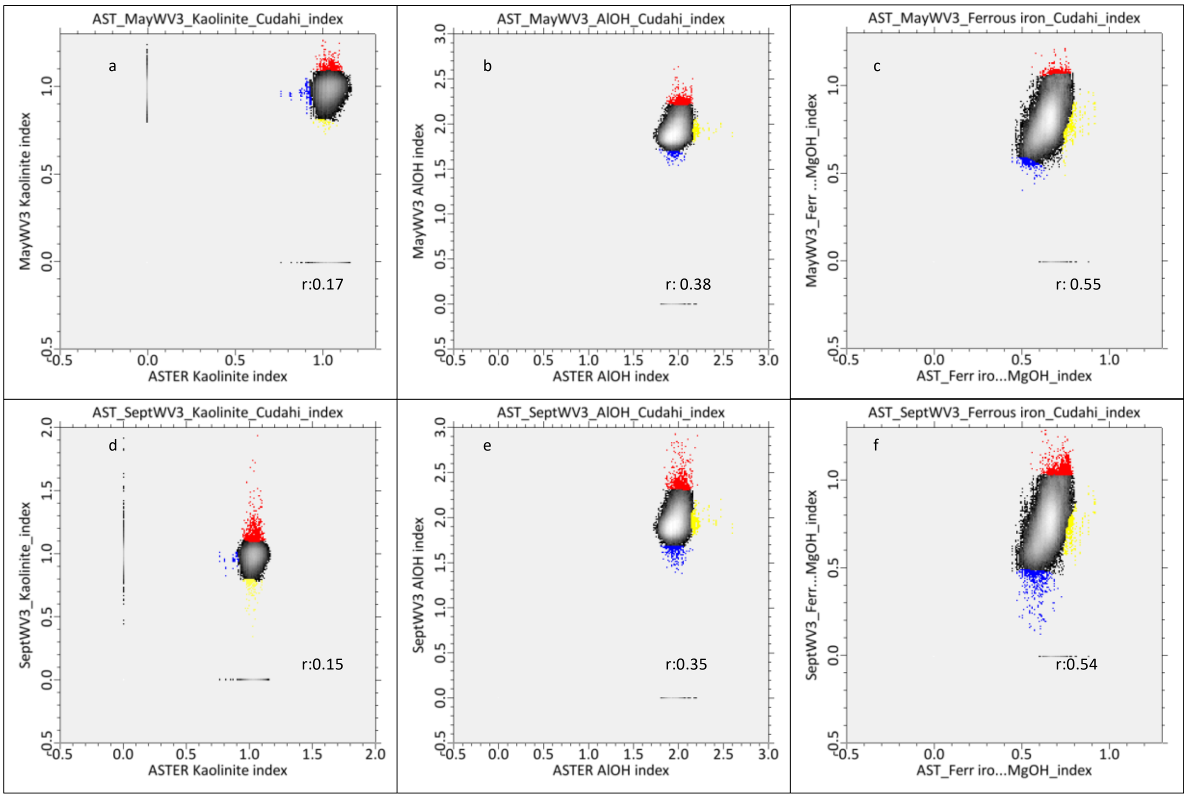

Figure 4.18 Scatter plots of band ratios defined by Cudahy. a-c compare ASTER to MayWV-3 while d-f compares ASTER to SepWV-3. The red colours are areas (pixels) with high values for the index on the y-axis, and the yellow colour are areas (pixels) with high values for the index on the x-axis. They indicate pixels that match with the index spectra and spatially on the ratio maps indicates areas of the alteration. The blue colour indicates pixel with low values and do not represent the index mineral.

Plots a and d show no correlations between ASTER and WV-3. ASTER pick up very low content compared to WV3 in kaolinite. For AlOH, there is also no correlation. They both have different peaks; the red colour marks the peak of WV-3 while the yellow colour marks the peak of ASTER. The red coloured pixels, when plotted over the index maps, match the known alteration areas. While the yellow peak corresponds to the areas along the coast. In case of ferrous iron, the images are moderately correlated.

The clouds of high and low densities in the scatter plots were thresholded and exported onto the respective ratio image to see their locations on the images. Mean spectra were collected for confirmation of the representation of the index. The results are displayed in figures 4.19 – 4.21.

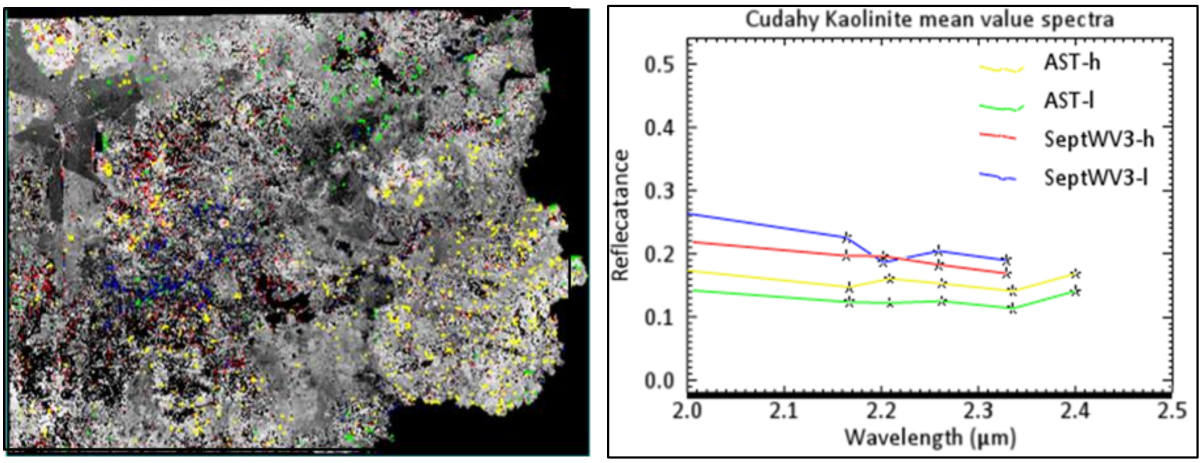

Figure 4.19 High and low pixels values for Kaolinite in ASTER and September acquisition with respective mean spectra calculated using Cudahy algorithm. The red and yellow spectra represent the pixels with high values for WV-3 and ASTER respectively. The blue represents pixels with low values for WV-3 and green represent pixels with low values for ASTER. This indicates very poorly or no correlations between ASTER and WV-3.

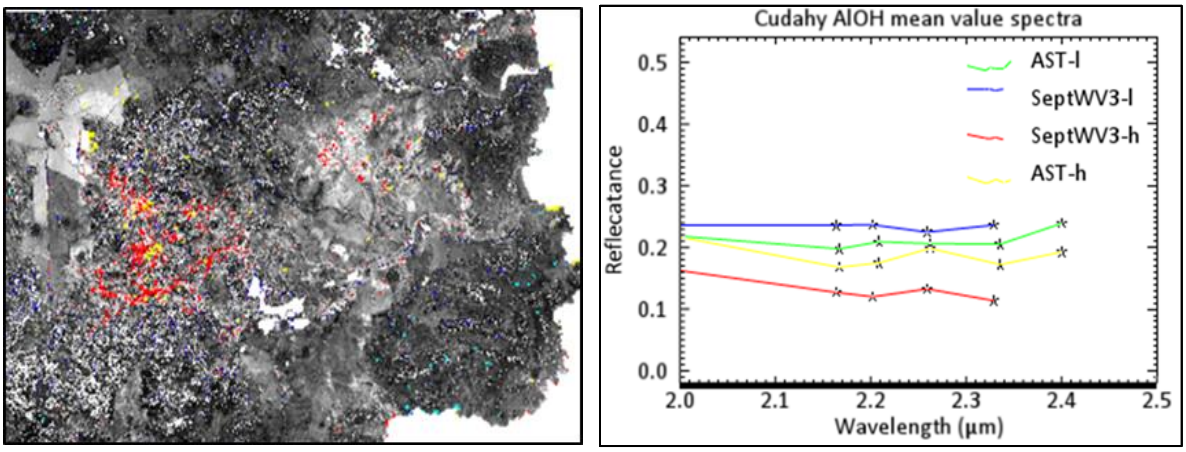

Figure 4.20 High and low pixels values for AlOH in ASTER and September acquisition with respective mean spectra calculated using Cudahy algorithm. The red and yellow spectra represent the pixels with high values for WV-3 and ASTER respectively. The blue represents pixels with low values for WV-3 and green represent pixels with low values for ASTER. This indicates low correlations between ASTER and WV-3.

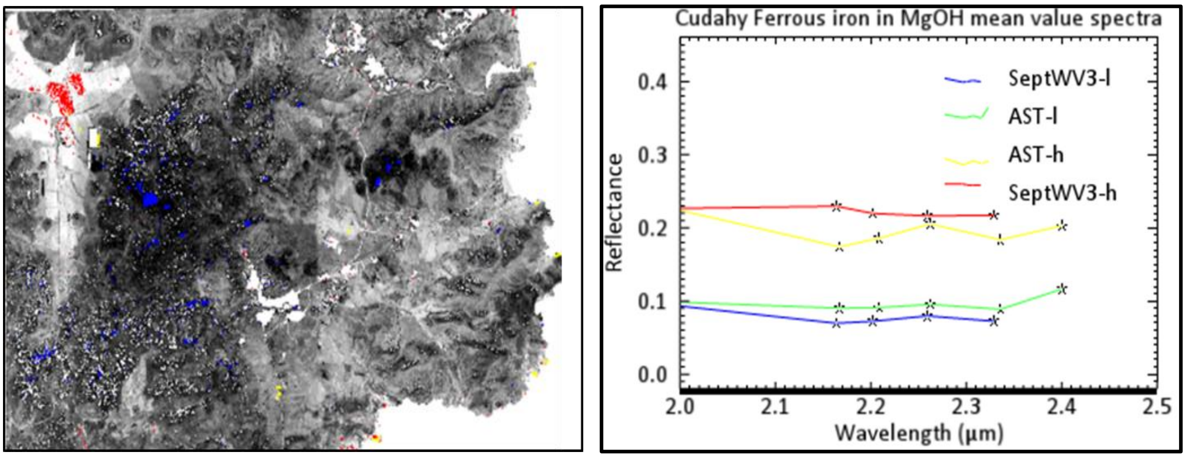

Figure 4.21 High and low pixels values for ferrous iron content in MgOH/carbonate in ASTER and September acquisition with respective mean spectra calculated using Cudahy algorithm. The red and yellow spectra represent the pixels with high values for WV-3 and ASTER respectively. The blue represents pixels with low values for WV-3 and green represent pixels with low values for ASTER. This indicates moderate correlations between ASTER and WV-3.

4.3.4. Resampled ASTER versus resampled WV-3.

HyMAP was resampled spectrally to both ASTER and WV-3. At 4m resolutions, band ratios were calculated on the resampled images, and the results show good correlations between the resampled images (Figure4.22).

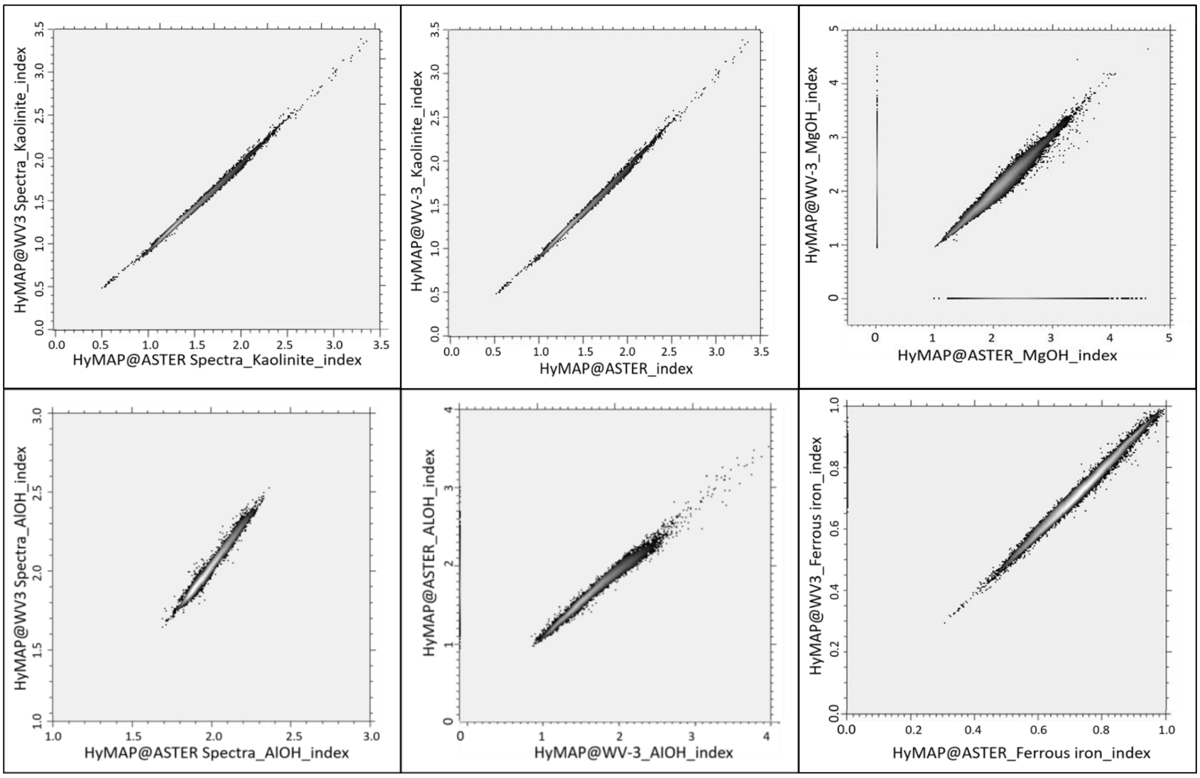

Figure 4.22 Correlations of simulated ASTER and WV-3 at 4m HyMAP spatial resolutions. The images are at their actual spectral resolutions, but all are at 4m spatial resolutions which shows the above correlations

4.4 Topographic illumination effects on ASTER SWIR results.

The results of ASTER index products for kaolinite (Figure 4.4a) appeared to be noisy as compared to the ASTER resampled HyMAP (Figure 4.4e). Following reports of previous studies (Hewson et al., 2005; Hewson & Cudahy, 2011) on the crosstalk effects on ASTER SWIR bands, topography illumination effects were examined.

Using the ASTER DEM product, shaded relief topography was generated to simulate the artificial sun illumination at the sun angles at the time of the ASTER acquisition (6th May 2004). Figures 4.23 & 4.24 show the comparison between the shaded relief and the ASTER kaolinite and AlOH products. The figures show a correlation between the dark areas and the index products in yellow as low value and red as high values of the kaolinite and AlOH.

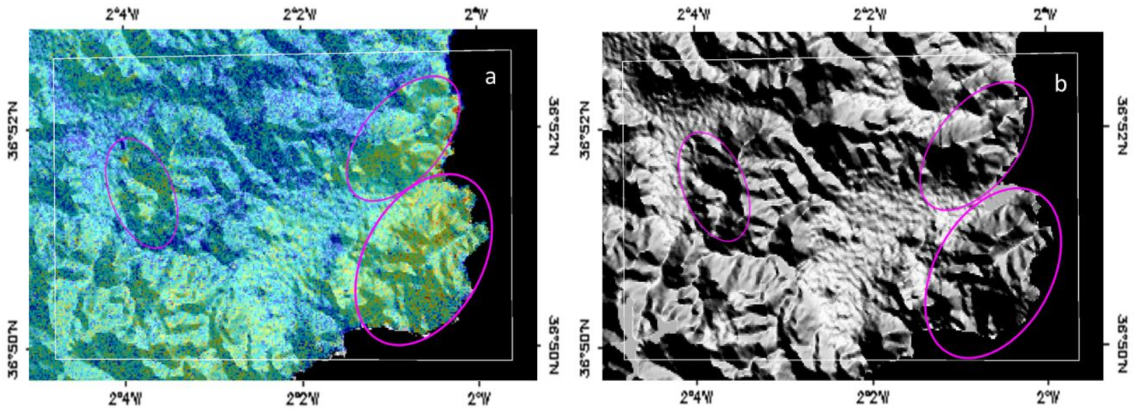

Figure 4.23 (a) Kaolinite abundance derived from crosstalk corrected surface reflectance data draped over sun-illuminated ASTER DEM (Elevation 66°, Azimuth 143°). The pink circles highlight the index product (yellow and red) in association with dark (shadows)area. (b) Sun illuminated DEM of the area; the pink circles indicate areas of low albedo associated with the crosstalk effect.

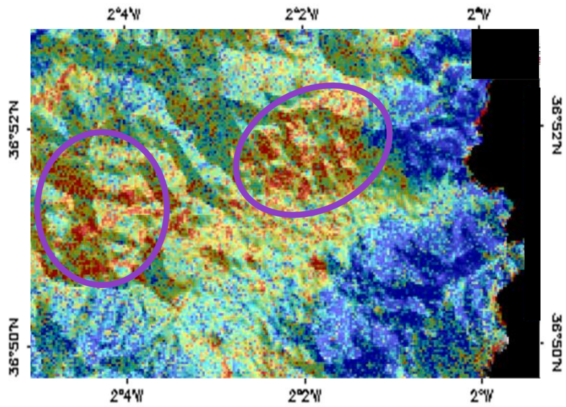

Figure 4.24 AlOH abundance derived from crosstalk corrected surface reflectance data draped over sun-illuminated ASTER DEM (Elevation 66°, Azimuth 143°). The pink circles highlight the index product (red) in association with dark (shadows)area.

5. DISCUSSION

The capabilities of ASTER and WV-3 for mineral mapping were studied and compared in application to an epithermal alteration system. Two sets of comparison were made: First a comparison of two different sensors ASTER and WV-3 to find out an optimal spectral and spatial resolution to discriminate certain mineral(s). These datasets (ASTER and WV-3) were chosen in order to highlight the potential of WV-3 in providing data continuity for ASTER at a higher spatial resolution, and also for their availability to this research. Second is a comparison of two different acquisition dates (May and September 2017) by the same sensor WV-3 to examine how differences that occur over time, such as sunlight and vegetation cover affects the mapping of the selected alteration minerals.

A band ratio approach was used as a basis for the comparison. Furthermore, scatter plot and statistics were used for more detailed comparisons. Six mineral indices which are typical of the study area were selected, and the results are discussed in section 5.4.

5.1. Vegetation cover in the area

The NDVI calculated for the ASTER, HyMAP and the two WV-3 scenes (Figure 4.2) showed some variations of the vegetation cover in the images. ASTER and HyMAP images were acquired in the same month (May,6 and 18) and the same year (2004). It was expected that they would have a same green cover, but some differences were observed. This is evident in the scatter plot (Figure 4.3b) and the correlation coefficient of 0.44. However, mean NDVI of the ASTER (0.28) and HyMAP (0.27) shows close similarity. The variations observed could be as a result of the difference in the sensor's signal to noise ratio behaviour, sun angle, and or atmospheric conditions (e.g. water moisture) that influence spectral products including the NDVI. In the May and September scenes of WV-3, the vegetation cover in the images also looked similar to the correlation coefficient of 0.49. However, a slight difference is observed in the mean values (0.224 and 0.223) of the scenes, the population peaks on the scatter plots which are not on the 1-1 relationship.

The sensors have different sun elevation angles, nadir position and distance to the ground, and viewing angle (Table 2.2). These have influence in spectral products including NDVI and could be the reasons for the differences observed in the images. On the other hand, the weather history of the area (Appendices I-III) from two weather stations, Almeria on the southwest and Carboneras in the northeast (Figure 2.2) showed the same conditions for Rodalquilar in both 2017 and 2004. The temperature difference can result in varying evapotranspiration (directly into the atmosphere) in the two periods which can influence the NDVI values. A study in Bangladesh has indicated a good correlation of NDVI with total evapotranspiration (Islam et al., 2015).

In general, the area was more vegetated at the time of ASTER acquisition (2004) than at the time of WV-3 acquisition (2017). NDVI >0.4 were masked to suppress effects of vegetation in the analysis of the images. However, Bedini et al., (2009), Mielke et al., (2016) and Yokoya et al., (2016) reported a wide spread of non-photosynthetic vegetation in the area. The dry vegetation has cellulose absorptions which can cause spectral mixing with mineral absorptions features (Rockwell, 2012), particularly with SWIR wavelength.

5.2. ASTER and WV-3 instrumentations

The two sensors have the similarity that they both have multi-spectral bands in the VNIR and SWIR ranges of the electromagnetic spectrum (Figure1.1 & Table 1.1) and are used for geological applications. However, they differ in both spectral and spatial resolutions. ASTER has three bands in VNIR and six bands in the

SWIR, whereas WV-3 has 8 bands in the VNIR and 8 bands in the SWIR. Importantly, WV-3 has bands that cover the 0.9μm and 1.2μm iron absorption features, which ASTER do not have. On the other hand, ASTER has band 9 that covers the 2.360 -2.430μm beyond the SWIR8 (2.295 – 2.365μm) of WV-3. The 2.360 -2.430μm wavelength is important for mapping carbonate minerals. Also, ASTER has bands in the thermal infrared region of the spectrum that is useful for mapping silicate minerals which WV-3 is deficient in, but this research did not include these regions. Spatially, WV-3 has higher spatial resolutions 1.2m in the VNIR and 7.5m in the SWIR, in contrast to the 15m in the VNIR and 30m in the SWIR of ASTER.

The ASTER and WV-3 images have different acquisition dates May 2004 and May 2017. To distinguish sensors differences from temporal differences, the two sensors were spectrally simulated by HyMAP (acquired May 2004) and vegetation in the real and simulated images was masked. To avoid introduction of artifacts, buildings, water ponds and ocean was masked (manually) as well.

5.3. The algorithm used in the comparison

The two sets of algorithms applied (Tables 3.1 and 3.2) were each originally defined for a particular sensor. The Cudahy algorithm (Cudahy, 2012) were defined 'with Australian conditions' for ASTER. The algorithm has default thresholds and stretch type which were all defined based on the Australian experience. The second set of algorithms defined by Sun et al., (2016), were originally for WV-3 and no thresholds were specified. The two algorithms used different bands combinations to highlights the absorption features of the mineral indices. For that reason, and the differences in the band positions of each sensor, some definition can only be applied to the sensor it was originally designed for.

To compare ASTER with WV-3, six index definitions that have corresponding bands in both sensors were used. Kaolinite, AlOH, and ferrous iron content in MgOH indices defined by Cudahy and kaolinite, AlOH and MgOH indices definitions by Sun et al. The idea here was to see how a sensor interprets a particular index by the two algorithms. It will be noticed that, in the Cudahy selected indices, ferrous iron content in MgOH was selected instead of MgOH, even though the intention was to have corresponding indices from both algorithms. This is because the MgOH bands combinations by Cudahy include band 9 which WV-3 is deficient. Furthermore, Sun et al defined an index for jarosite that cannot be applied to ASTER, because ASTER did not have a corresponding band for the VNIR6 band of WV-3. Jarosite can be discriminated under the FeOH group, and Cudahy algorithm for FeOH can be applied for both ASTER and WV-3 images. In the case of comparing the May 2017 with September 2017 acquisitions of WV-3, the indices definitions by Sun et al were used. This is because the algorithm was originally defined for the WV-3 and all indices can be tested on both images.

Figures 4.4 & 4.5 show the results of the Cudahy and the Sun et al definitions respectively. The spectra were compared with ASD field spectra collected (Figures 4.6). Also, the index product images were compared with the established alteration map of the area, published by Arribas et al (1995) (Figure 2.1c).

5.4. The mineral indices

Kaolinite

With the Cudahy algorithm, using HyMAP as a control, the kaolinite index was poorly discriminated in all images: ASTER, the May and September scenes of WV-3, and the ASTER and WV-3 images simulated by HyMAP (Figure 4.4a-f). Within the kaolinite product derived from ASTER image (Figure 4.3a), the prediction is more intense compared to WV-3 (Figures 4.4 b-c). However, the results are noisy, and little of the known kaolinite alteration zones was highlighted (Figure 4.4a). The kaolinite bearing prediction by the ASTER was more to the south east of the study area, an area underlaid by andesites, reef complex and volcanic sequence (Figure 5.1a). These noisy kaolinite anomalies observed in the original ASTER image was not seen in the simulated ASTER image when using the Cudahy algorithm. On the simulated image, the prediction was highlighting the alteration zones, but less intense. The noise can be attributed to the image spatial resolution (15m) which could help increase the complications from spectral mixing. Since the simulated ASTER at 4m spatial resolution does not show the same noisy anomalous pattern, potential issues that need to be considered or eliminated could include: differences in sensor signal to noise (SNR), ASTER SWIR Crosstalk (Iwasaki et al., 2002), spectral mixing for pixels at 30 versus 4 metres, temporal vegetation/moisture changes, and variable illumination conditions. Hewson & Cudahy (2011) and Hewson et al (2005) reported on the presence of a “crosstalk effect” in ASTER SWIR bands. Mostly affected are Bands 5 & 9 because of their proximity to band 4(Iwasaki, Fujisada, Akao, Shindou, & Akagi, 2002). The ASTER data used in this research was crosstalk corrected with software, but previous studies have reported the presence of a residual effect in some data scenes. For this, the relationship between the ASTER product and topography was examined (section 4.4). A shaded relief topography in figure 4.23 highlights a correlation between dark areas and the noisy interpretation, suggesting a crosstalk effect. Although not all the dark areas are covered by the noisy anomalies, but there are anomalous results in some shadows. The low illumination (shadow) areas enhance the false SWIR crosstalk anomalies, a similar case identified by Hewson et al (2005) in ASTER data over an area nearby Broken Hill mining district. This effect was not apparent in the resampled ASTER by HyMAP and not a problem in the WV-3 image. Furthermore, another possible reason for the noisy pattern could be the presence of dry vegetation, and or mafic mineral which in an AlOH poor area causes difficulty in discriminating the index (Cudahy, 2012).

It should be noticed that within the simulated ASTER (Figure 4.4e), the two main alteration zones and the abundance stage 2 alunite were more clearly delineated than it is in the original ASTER image (Figure 4.4a). This could be in addition to the crosstalk effect in the ASTER, and spatial resolutions (4m & 15m) difference, a result of the close similarity in absorption feature of the kaolinite and alunite, which in most cases with multispectral images resulting to an overlap in the interpretation. Kaolin group minerals have a characteristic spectral absorption wavelength of 2.16-2.2µm, corresponding to the SWIR5 & SWIR6 of WV-3, and band 5 & 6 of ASTER. This region is important for highlighting both argillic and advance argillic alterations minerals such as kaolinite and alunite. Also, the absorption feature of kaolinite at band 5 typically showed that both minerals could be discriminated by the argillic and advanced argillic indices (Rockwell, 2012). They can both be discriminated by either simple band ratio or relative band depth index. The distinguishing feature between them is the deepest part of the absorption feature: Kaolinite has the deepest feature at band 6 while alunite has it at band 5. A spectral mixture of these two materials can occur in an area of sparse, dry vegetation that is underlain by kaolinite, as explained in (Rockwell, 2012). ASTER SWIR at 30m spatial resolution is more vulnerable than WV-3 at 7.5m and HyMAP at 4m. The dry vegetation has cellulose absorptions at ASTER bands 5,7& 8 when this mixes with the mineral, the resultant spectra resemble that of alunite (Rockwell, 2012).

Comparing the ratio products of the May and September WV-3 scenes (Figure 4.4 b&c) with HyMAP ratio product and the Arribas alteration map (Figures 4.4d & 2.1c respectively), the discrimination of the kaolinite is lower in May than in September acquisition. Applying it on WV-3 simulated HyMAP (Figure 4.4f), the result looks quite similar to the original WV-3 image that was acquired 9th /09/2017 (Figure 4.4c).

Using the Sun et al algorithm, kaolinite could be discriminated more clearly in all images (Figure 4.5 a-f) as compared to the Cudahy algorithm in figure 4.4 a-f. Point to note and investigate further is that, the Sun et al algorithm predicts the alteration in the ASTER image more closely to the established Arribas alteration map of the area (Figure 2.1c) as compared to the Cudahy algorithm, which was originally defined for ASTER. However, the stretches and thresholds that were applied when using the Cudahy definitions were the designed ones as applied for the Australian wide ASTER compositional map products (Cudahy, 2012; https://data.gov.au/dataset/national-aster-map-of-australia).

The kaolinite prediction by the two sensors differs, using the Cudahy algorithm, it was colour intense in ASTER but noisy as it gives anomalies in areas outside the alteration zones. While in WV-3, it was less colour intense and less noisy. Spectral overlap was also observed between kaolinite and alunite, and both can be discriminated by either simple band ration or relative band depth. A seasonal change sensitivity by kaolinite was noticed between the May and September interpretations.

AlOH

The results of the AlOH ratio using Cudahy algorithm (Figure 4.4) generally showed poor discrimination of the index when compared to Suns' algorithm (Figure 4.5) and to the established alteration map (Figure 2.1c). On the images in figure 4.4, the prediction by ASTER and May WV-3 (Figures 4.4 a&b) were less intense as compared to September WV-3 scene and HyMAP (Figures 4.4 c&d) interpretations. The September scene of WV-3 and HyMAP ratio products correspond much closer to the alteration map in figure2.1c. Comparing the simulated ASTER and WV-3 in figures 4.4 e&f with figure 2.1c shows that WV-3 interpreted the AlOH better than ASTER using Cudahy algorithm. The crosstalk effects of ASTER in shadowed areas was still an issue (Figure 4.24) as compared to WV-3 and simulated ASTER by HyMAP. Comparing the May and September scenes of WV-3 using original HyMAP (Figures 4.4 b-d) as a control, the index was better discriminated in the September scene. These are scenes of the same sensor, but there are differences in their nadir position, sun elevation and ground sampling distance (Table 2.2). These in addition to the difference in the vegetation cover could be the factor(s) for the difference in the prediction. The discrimination in September scene is quite similar to the interpretation in HyMAP image. Although the September scene could not pick up the stage 2 alunite zone as in the HyMAP. This similarity is an indication of favourable conditions in September scene for the discrimination of the index.

Using Suns' algorithm, the AlOH index is less discriminated in ASTER as compared to both WV-3 images (Figure 4.5 a-c). Examining the distribution of high and low values taken from the scatter plot of ASTER *versus* WV-3 on the ratio image (Figure 4.16), the WV-3 high values match well with the alteration zones while the high values of ASTER appear noisy and are scattered all over. Very few of the ASTER high values matched with the alteration zones, the majority are located in areas with carbonate mineral occurrences. It could be as a result of the large pixel size of ASTER that resulted in a mixed pixel and averaging out of spectra. This is observed in ASTER spectra high value (yellow) in figure 4.16 in which the absorptions at 2.17μm and 2.209μm were dominated by the absorption at 2.337μm. Comparing the spectrally resampled images of ASTER and WV-3 by HyMAP at the original 4m spatial resolution of HyMAP, the results appeared pretty similar (Figures 4.5 e&f). This signifies effect of spatial resolution in the interpretations, ASTER at 15m and at 4m of HyMAP predicts the AlOH differently (Figure 4.5 a&e), and WV-3 at 1.2m and at 4m of HyMAP predicts very similarly.

Overall, the AlOH index prediction with the Sun et al algorithm (Figure 4.5a) is less noisy compared to the result using Cudahy algorithm (Figure 4.4a). It has similar patches (although smaller in size) of the alterations as predicted by HyMAP (Figure 4.5d), which matches with the alteration zones published by Arribas (Figure 2.1c). It is observed that both spatial and spectral resolutions influence the index. This is noticeable between Sept WV-3 with 16 bands at 1.2m, which discriminates very similar to HyMAP with 126 at 4m. The same can be seen between simulated ASTER with 9 bands at 4m and simulated WV-3 with 16 bands at 4m. Both ASTER and WV-3 were resampled to the same spatial resolutions (4m) of HyMAP, but with different spectral resolutions, the simulated WV-3 with the higher spectral resolutions discriminates better. Furthermore, seasonality difference seems to have an influence on the detection of the index as can be seen between May and September WV-3 images; it is better discriminated in September than in May. Although the acquisition sun angle is less in September (Table 2.2), may be the atmospheric issues (e.g. low humidity) were less an issue.

Ferrous iron content in MgOH/carbonate

The Sun et al algorithms did not provide for this index; it was only defined by Cudahy. The algorithm worked on all images well, and the results looked relatively similar (Figure 4.4). The ratio product from the two WV-3 original images were spatially very comparable. Comparing the WV-3 with ASTER showed some variations in the northern and western parts of the scenes. The WV-3 overestimates to the west (agricultural field), and ASTER overestimates to the north (Figures 4.4 a-c). Comparing the ratio maps with the NDVIs maps (Figure 4.2) of each image suggests a possible influence by the presence of green vegetation in the ASTER/WV-3 differences of the Ferrous iron in MgOH/carbonate product. The influence of green vegetation can be confirmed when examining the result on the respective ASTER and WV-3 simulated HyMAP. The results looked very similar as there is no difference in the vegetation cover. The similarity of the images for the product is also evident in the scatter plots comparing them (Figure 4.18c). The ASTER and the two WV-3 images showed moderate correlation (0.55 and 0.54). Also, plots of the values clouds (high, low) on the ratio image supported the interpretation (Figure 4.21). The higher values of ASTER and WV-3 all fell around the same places and matched with the ratio interpretation; this is the same with the low values for the images. The index was interpreted very similarly by all the images, and it appeared to be less sensitive to seasonal variations.

MgOH

The Sun et al definition for this index provides bands combination that can be applied to both ASTER and WV-3. The ratio products appeared closely similar on all the six images (Figure 4.5 a-f). It seems to be insensitive to seasonality, looking at the appearance of the ratio product across the different seasons of the datasets. This similarity in the ratio product can be seen in figure 4.17 where high values (red & yellow) were related with a correlation value of 0.43 (Figure 4.14f). The high values were located around the same location, and that matches with the locations of the index product. However, the product looked slightly different in ASTER image (Figure 4.5a). The prediction appeared more pronounced to the north and southeast in ASTER than in the WV-3, and spatially in the central part, it interprets lesser than theWV-3. This could be the effect of the large pixel size of ASTER that could lead to spectral mixing. This difference is not seen in the ASTER, and WV-3 simulated HyMAP that are in the same spatial resolution (4m) of the HyMAP. Nevertheless, Cudahy (2012) mentioned that the interpretation of MgOH in ASTER is complicated with dry vegetation(redden), white mica and residual crosstalk effect. The area was noticed with non-photosynthesis plants (Figure 2.3 b&d). Also, previous works in the area reported having dry vegetation (Bedini et al., 2009; Mielke et al., 2016; & Yokoya et al., 2016). This with the residual crosstalk effect observed (Figure 4.23), can be related to the noisy pattern in the MgOH interpretation. The MgOH index product in the images is not distinct; this can be related to Hewson et al., (2005) studies where it was mentioned that MgOH mineral at ASTER SWIR spectral resolution could be confused with carbonate minerals.

Jarosite

This is another index defined by Sun et al, using bands VNIR6/SWIR7, of which ASTER does not have the corresponding VNIR6 (0.705-0.745) band. Therefore, this was only tested between the two scenes of WV-3. It was discriminated in both scenes but appeared to be more abundant in May acquisition than in September acquisition (Figure 4.12). The variation was evident in the scatter plot of the two which showed a very poor correlation (0.39). This suggests a susceptibility to seasonal change by the jarosite index. Spectra comparison of high values of jarosite in May and September images all matched with the field ASD and USGS-WV-3 resampled library (Figure 4.12). The location (waypoint 290 in appendix V) where the ASD field spectra were collected coincides with the area Ferrier (1999) mapped jarosite using Airborne Visible/Infrared Imaging Spectrometer (AVIRIS) and laboratory analysis. This confirmed that the algorithm could be used in mapping jarosite. Overall, the algorithm can be used to discriminate jarosite which is useful for environmental studies. The difference in abundance in the two scenes shows the index vulnerability to seasonal change.

Siderite

This is another index defined by Sun et al., using the band ratio combination VNIR8(0.860-1.040)/SWIR1(1.195-1.225) for mapping siderite carbonate. ASTER does not have the corresponding VNIR band, and therefore, this was only tested between the two WV-3 scenes. The spatial coverage of the index product in the ratio images, the scatter plot with a correlation coefficient of 0.28 and means values (May: 0.75, Sept: 0.70) showed that the prediction of the index product is slightly more in May than September. This suggests possible susceptibility of this product to seasonal change. This possibly related to vegetation effects from the incorporation of the VNIR band 8.

5.5. ASTER versus WV-3 images

Using HyMAP as a control, the kaolinite, AlOH, MgOH and ferrous iron content in MgOH/carbonate predicted by both ASTER and WV-3 revealed a contrast between the two images. The interpretations by ASTER were sometimes noisy, for instance, kaolinite and MgOH in figure 4.4a & 4.5a respectively. In cases where the interpretation is noise free, it only mapped small patches of the known alteration areas as seen for kaolinite and AlOH in figure 4.5 a&a respectively.

The spatial resolution of the images plays an important role in the prediction, as can be seen in the discrimination of kaolinite and AlOH by ASTER at 15m and simulated ASTER at 4m resolution. The effect of the spatial resolution in mineral mapping has also been studied by other authors: Hewson et al (2017) & Kruse et al (2011) emphasized the limitation of ASTRER's coarse spatial resolution in mineral mapping. Also, the issues related to the ASTER resolution was detailed in Hewson & Cudahy(2011). Other investigations on the resolution issues include; Yakowa et al (2016) where they fused EnMAP image at 30m with Sentinel-2 at 10m to have resolution enhanced EnMAP data at 10m. The spectral unmixing results by the EnMAP were comparable with the results from hyperspectral data at 10m (Yokoya et al., 2016). In another study, Kruse et al (2011) using simulated HyspIRI demonstrated the effects of reduced spatial resolution. In particular, Kruse et al (2011) showed the spectral effects of mineral mixing at reduced spatial resolution.

ASTER was noticed with spectral mixture of mineral groups such as AlOH and MgOH as can be seen in figure 4.16 & 4.17. For WV-3, the interpretation is noise free, and mostly matches with the known alterations extends. Spectrally, it can separate mineral groups as can be seen in figure 5.1. A colour composite of kaolinite, AlOH and ferrous iron in MgOH/carbonate for each data set was made (Figure 5.1). Both images predict the indices but at varying degrees.

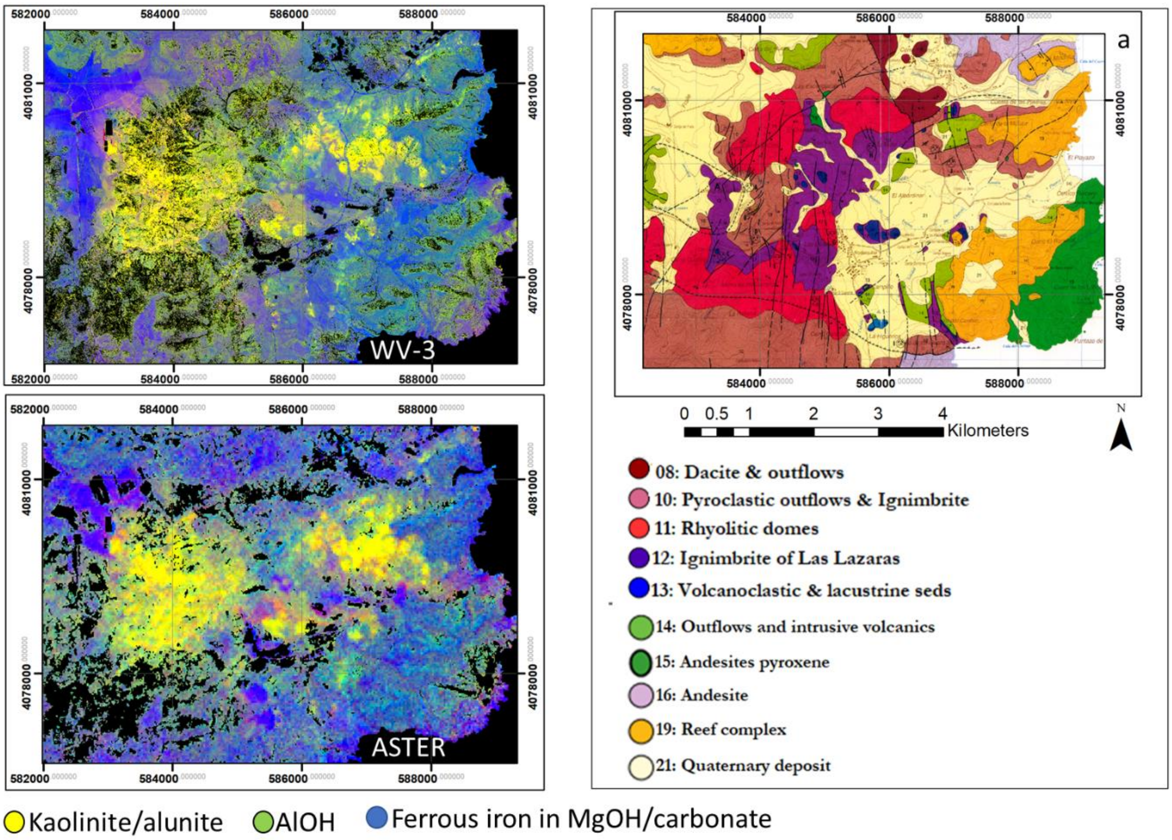

Figure 5.1 Colour composites made with WV-3 and ASTER images. (a) Geological map of Rodalquilar after Arribas 1993, and legend modified from van der Werff & van der Meer (2016). On the left, are colour composites made with WV-3 and ASTER images, the RGB consists of kaolinite, AlOH and Ferrous iron in MgOH/carbonate respectively. The yellow colour could be as a result close similarity of kaolinite and alunite that mixes red and green to yellow. The composite maps show how WV-3 image mimic the lithologic pattern in the established geological map. ASTER on the other hand barely discriminate the lithologies; it appeared to merge many groups.

5.6. May WV-3 versus September WV-3 images

Both scenes predict the mineral indices distinctly, the major difference between the two is in the abundance of the indices. Kaolinite and alunite products appeared to be more abundance in September scene, while jarosite index appeared to be more abundance in May scene, signifying a susceptibility to seasonal difference. While MgOH appeared to be less influence by the seasonal changes.

5.7. Cudahy algorithm versus Sun et al algorithm

Originally, the Cudahy algorithm was defined for ASTER while Sun et al for WV-3. The definitions that can be applied for both sensors were compared and showed that: Sun et al algorithm is effective on both images and performed optimally for kaolinite and AlOH. On the hand, Cudahy algorithm is less effective in the two images but has an optimal result for ferrous iron in MgOH/carbonate.

6. CONCLUSIONS AND RECOMMENDATIONS

6.1. Conclusion

The abilities of ASTER and WV-3 for mineral mapping were compared in the epithermal alteration system of Rodalquilar, Southeast Spain. In addition, two WV-3 scenes, acquired in May and September were compared as well. A band ratio approach was employed in the analysis of the datasets. The results led to the conclusions below, answering the research questions:

ASTER predictions were moderate as compared to the established alterations map, often complicated as observed in the interpretation of kaolinite which gives a noisy ratio index anomaly. Also, the large pixel size of ASTER. often resulted in mixed pixels as noticed in the analysis of the ASTER spectra, where AlOH spectral features were dominated by carbonate group (smectite).

- *Are there any minerals that are not discriminated and identified by ASTER but discriminated and identified by WV-3?*

  The WV-3 predictions matched the established geological map of the area, suggesting the WV-3 suitability for discriminating kaolinite, AlOH and MgOH indices. These findings offer suggestive evidence for WV-3 having an improvement in clay and iron bearing mineral mapping over ASTER. WV-3 discriminates jarosite while ASTER could not discriminate against it.

- *Given the spectral and spatial resolutions trade-off, which of the sensors will be preferred for iron-bearing, clay, and carbonate minerals mapping?*

  The WV-3 was able to mimic the established mineral map of the area, while ASTER discriminates few of the mineralogy. Therefore, WV-3 data have more advantages due to the radiation, spectral, and spatial resolution compared to ASTER data. It mapped iron bearing and clay minerals effectively and can map carbonates minerals such as dolomite and calcite, although ASTER's band at 2.4μm has an advantage for greater confidence. At this point, it can be emphasised that except for the carbonates minerals with diagnostic absorption feature at beyond 2.365μm and silicates minerals, WV-3 can effectively provide data continuity for ASTER.

- *Does the spatial resolution of WV-3 make a difference in the mineral discrimination as compared to an ASTER image?*

  The 30m SWIR of ASTER predicts less precisely the mineral indices as compared to the 7.5m SWIR of WV-3. The spatial resolution of the images plays an important role in the prediction, as can be seen in the discrimination of kaolinite and AlOH by ASTER and simulated ASTER at 4m resolution. Comparing the results of two sensors with results of HyMAP at 4m further proves the advantage of the spatial resolution as WV-3 and HyMAP results looks closely similar. This finding is consistent with previous researches such as Hewson & Cudahy(2011, 2012); (Yokoya et al., 2016) and Kruse et al., (2011) on the issue of low spatial resolution in mineral mapping.

- *Does the seasonal variation of the year affect the identification of alteration minerals from the same sensor? and*
- *Is any of the index product sensitive to seasonality?*

  There is difference in the interpretations of the two scenes of WV-3 acquired in summer and early spring. Kaolinite and AlOH were more abundant according to the spectral indices in the September scene of WV-3 than in the May scene. Jarosite, on the other hand, is displayed with higher index values in the May than in the September scene. The kaolinite, AlOH and jarosite appeared to be susceptible to seasonal variation as observed in the index ratio results of May and September 2017 scenes of WV-3. While MgOH is less sensitive to the seasonal changes.

- *Do I need a particular season of the year for optimum identification of specific mineral product(s)?*
  The data analysed were just two temporal imagery, and these are not enough for seasonal analysis.

6.2. Recommendation

However, this research focused on the aspects that the two datasets ASTER and WV-3 have in common except for the difference in spatial resolutions that was considered as well. They differ in wavelength coverages, ASTER covers part of the thermal infrared region while WV-3 only covers visible and shortwave ranges. Also, within the visible and shortwave ranges, ASTER don't have band covering the 1.2 and 0.9 regions while WV-3 don't have band covering 2.365 - 2.4μm. These are important regions for iron bearing minerals, MgOH and carbonate mapping respectively. Furthermore, for the seasonal difference analysis of the same sensor, only two acquisitions (not enough) of WV-3 were available. To this end, the following recommendations were made for the improvement or expansion of this research:

- For further application of band ratio using Cudahy algorithm to ASTER data, an attempt should be made to determine stretch limits based on scene characteristics since the defaults were derived based on Australian ASTER experience.

- To fully understand the optimal time of a year for mapping certain minerals, more acquisitions need to be compared.

REFERENCES

Arribas, A. (1993). Mapa Geological del Distrito Minero de Rodalquilar, Almeria, Scale 1-25000. Instituto Tecnologico Geominero de Espano: Madrid, Spain, 1993.

Arribas, A. (1995). Characteristics of high-sulfidation epithermal deposits, and their relation to magmatic fluid. In *Magmas, Fluids, and Ore Deposits* (Vol. 23).

Asadzadeh, S., & de Souza Filho, C. R. (2016). A review on spectral processing methods for geological remote sensing. *International Journal of Applied Earth Observation and Geoinformation*, *47*, 69–90. https://doi.org/10.1016/j.jag.2015.12.004

Bedini, E., van der Meer, F., & van Ruitenbeek, F. (2009). Use of HyMap imaging spectrometer data to map mineralogy in the Rodalquilar caldera, southeast Spain. *International Journal of Remote Sensing*, *30*(2), 327–348. https://doi.org/10.1080/01431160802282854

Clark, R. N. (1999). Spectroscopy of Rocks and Minerals, and Principles of Spectroscopy. In *Remote Sensing for the Earth Sciences, (A.N. Rencz, ed.)* (pp. 3–58). New York: John Wiley and Sons.

Cocks, T., Jenssen, R., Stewart, A., Wilson, I., & Shields, T. (1998). The HyMap airborne hyperspectral sensor: the system, calibration and performance. *Proceedings of the 1rd EARSeL Workshop on Imaging Spectrometry*, 37–42.

Cudahy, T. J. (2012). *Satellite ASTER Geoscience Product Notes for Australia.*

Dubey, S., Gupta, Y. K., & Soni, D. (2016). Comparative Study of Various Segmentation Techniques with their Effective Parameters. *International Journal of Innovative Research in Computer and Communication Engineering*, *4*(10). https://doi.org/10.15680/IJIRCCE.2016.

Ferrier, G. (1999). Application of imaging spectrometer data in identifying environmental pollution caused by mining at Rodaquilar, Spain. *Remote Sensing of Environment*, *68*(2), 125–137. https://doi.org/10.1016/S0034-4257(98)00105-9

Hecker, C., Van Der Werff, H., Kooistra, J., Van Der Meijde, M., & Van Der Meer, F. (2007). Thresholding of Classification Rule Images – How Much is Enough? In *Proceedings 5th EARSeL Workshop on Imaging Spectroscopy*.

Hewson, R., & Cudahy, T. (2011). Issues Affecting Geological Mapping with ASTER Data: A Case Study of the Mt Fitton Area, South Australia (Vol. 11). https://doi.org/10.1007/978-1-4419-6749-7

Hewson, R. D., Cudahy, T. J., Mizuhiko, S., Ueda, K., & Mauger, A. J. (2005). Seamless geological map generation using ASTER in the Broken Hill-Curnamona province of Australia. *Remote Sensing of Environment*, *99*(1–2), 159–172. https://doi.org/10.1016/j.rse.2005.04.025

Hewson, R., Robson, D., Carlton, A., & Gilmore, P. (2017). Geological application of ASTER remote sensing within sparsely outcropping terrain, Central New South Wales, Australia. *Cogent Geoscience*, *3*(1), 1–22. https://doi.org/10.1080/23312041.2017.1319259

Inzana, J., Kusky, T., Higgs, G., & Tucker, R. (2003). Supervised classifications of Landsat TM band ratio images and Landsat TM band ratio image with radar for geological interpretations of central Madagascar. *Journal of African Earth Sciences*, *37*(1–2), 59–72. https://doi.org/10.1016/S0899-5362(03)00071-X

Islam, M. M., Mainul, M., & Mamun, I. (2015). Variations of NDVI and Its Association with Rainfall and Evapotranspiration over Bangladesh. *Rajshahi University Journal of Science & Engineering ISSN*, *43*, 2309–952.

Iwasaki, A., Fujisada, H., Akao, H., Shindou, O., & Akagi, S. (2002). Enhancement of spectral separation performance for ASTER/SWIR. *International Symposium on Optical Science and Technology*, *4486*, 42–50. https://doi.org/10.1117/12.455140

Jourdan, F., Paris, A., Koenig, P.-Y., & Melançon, G. (2007). Multiscale Scatterplot Matrix for Visual and Interactive Exploration of Metabonomic Data. *Pixelization Paradigm*, *4370*, 202–215. https://doi.org/10.1007/978-3-540-71027-1

Karungan, D., & Sujatha, N. (2017). Survey on Various Image Segmentation Techniques. *JETIR1702025 Journal of Emerging Technologies and Innovative Research*, *4*.

Kruse, F. A., Baugh, W. M., & Perry, S. L. (2015). Validation of DigitalGlobe WorldView-3 Earth imaging satellite shortwave infrared bands for mineral mapping. *Journal of Applied Remote Sensing*, *9*(1), 96044. https://doi.org/10.1117/1.JRS.9.096044

Kruse, F. A., & Perry, S. L. (2009). Improving multispectral mapping by spectral modeling with hyperspectral signatures. *Journal of Applied Remote Sensing*, *3*(1), 33504. https://doi.org/10.1117/1.3081548

Kruse, F. A., Taranik, J. V., Coolbaugh, M., Michaels, J., Littlefield, E. F., Calvin, W. M., & Martini, B. A. (2011). Effect of reduced spatial resolution on mineral mapping using imaging spectrometry-examples using hyperspectral infrared imager (HyspIRI)-simulated data. *Remote Sensing*, *3*(8), 1584–1602. https://doi.org/10.3390/rs3081584

Langford, R. L. (2015). Temporal merging of remote sensing data to enhance spectral regolith, lithological and alteration patterns for regional mineral exploration. *Ore Geology Reviews*, *68*, 14–29. https://doi.org/10.1016/j.oregeorev.2015.01.005

Mielke, C., Rogass, C., Boesche, N., Segl, K., & Altenberger, U. (2016). EnGeoMAP 2.0-automated hyperspectral mineral identification for the German EnMAP space mission. *Remote Sensing*, *8*(2). https://doi.org/10.3390/rs8020127

Mookambiga, A., & Gomathi, V. (2016). Comprehensive review on fusion techniques for spatial information enhancement in hyperspectral imagery. *Multidimensional Systems and Signal Processing*, *27*(4), 1–27. https://doi.org/10.1007/s11045-016-0415-2

Mustard, J. F., & Sunshine, J. M. (1999). 5 Spectral Analysis for Earth Science: Investigations Using Remote Sensing Data. In *Remote Sensing for Earth Sciences*. John Wiley & Sons, Inc.

Oak, R. (2016). A Study of Digital Image Segmentation Techniques. *International Journal Of Engineering And Computer Science*, *5*(12), 19779–19783. https://doi.org/10.18535/ijecs/v5i12.76

Oyarzun, R., Cubas, P., Higueras, P., Lillo, J., & Llanos, W. (2009). Environmental assessment of the arsenic-rich, Rodalquilar gold-(copper-lead-zinc) mining district, SE Spain: Data from soils and vegetation. *Environmental Geology*, *58*(4), 761–777. https://doi.org/10.1007/s00254-008-1550-3

Richards, J. A. (2013). *Remote Sensing Digital Image Analysis*. *Methods* (Fifth). London: Springer Heidelberg. https://doi.org/10.1007/3-540-29711-1

Rockwell, B. W. (2012). *Description and Validation of an Automated Methodology for Mapping Mineralogy , Vegetation , and Hydrothermal Alteration Type from ASTER Satellite Imagery with Examples from the San Juan Mountains , Colorado. Scientific Investigations Map 3190*. Reston, Virginia.

Rytuba, J. J., Arribas, A., Cunningham, C. G., McKee, E. H., Podwysocki, M. H., Smith, J. G., … Arribas, A. (1990). Mineralized and unmineralized calderas in Spain; Part II, evolution of the Rodalquilar caldera complex and associated gold-alunite deposits. *Mineralium Deposita*, *25*(1), 29–35. https://doi.org/10.1007/BF00205247

Saleh Al-Amri, S., Kalyankar, N. V, & Khamitkar, S. D. (2010). Image Segmentation by Using Thershod Techniques. *Journal of computing*, *2*(5), 2151–9617.

Sun, Y., Tian, S., & Di, B. (2016). Extracting mineral alteration information using WorldView-3 data. *Geoscience Frontiers*, 1–12. https://doi.org/10.1016/j.gsf.2016.10.008

van der Meer, F. (2004). Analysis of spectral absorption features in hyperspectral imagery. *International Journal of Applied Earth Observation and Geoinformation*, *5*, 55–68. https://doi.org/10.1016/j.jag.2003.09.001

van der Meer, F. (2006). The effectiveness of spectral similarity measures for the analysis of hyperspectral imagery. *International Journal of Applied Earth Observation and Geoinformation*, *8*(1), 3–17. https://doi.org/10.1016/j.jag.2005.06.001

van der Meer, F. D., van der Werff, H. M. A., & van Ruitenbeek, F. J. A. (2014). Potential of ESA's Sentinel-2 for geological applications. *Remote Sensing of Environment*, *148*, 124–133. https://doi.org/10.1016/j.rse.2014.03.022

van der Meer, F. D., van der Werff, H. M. A., van Ruitenbeek, F. J. A., Hecker, C. A., Bakker, W. H., Noomen, M. F., Woldai, T. (2012). Multi- and hyperspectral geologic remote sensing: A review. *International Journal of Applied Earth Observations and Geoinformation*, *14*, 112–128. https://doi.org/10.1016/j.jag.2011.08.002

van der Werff, H., & van der Meer, F. (2015). Sentinel-2 for mapping iron absorption feature parameters. *Remote Sensing*, *7*(10), 12635–12653. https://doi.org/10.3390/rs71012635

Yokoya, N., Chan, J. C. W., & Segl, K. (2016). Potential of resolution-enhanced hyperspectral data for mineral mapping using simulated EnMAP and Sentinel-2 images. *Remote Sensing*, *8*(3). https://doi.org/10.3390/rs8030172

Zitová, B., & Flusser, J. (2003). Image registration methods: A survey. *Image and Vision Computing*, *21*(11), 977–1000. https://doi.org/10.1016/S0262-8856(03)00137-9

APPENDICES

Appendix I

1st Feb – 30th May, 2004 Weather history from Almeria weather station

	Max	Avg	Min	Sum
Temperature				
Max Temperature	**27** °C	**18** °C	**12** °C	
Mean Temperature	**22** °C	**15** °C	**7** °C	
Min Temperature	**19** °C	**12** °C	**3** °C	
Degree Days				
Heating Degree Days (base 65)	20	7	0	835
Cooling Degree Days (base 65)	6	0	0	37
Growing Degree Days (base 50)	21	9	0	1032
Dew Point				
Dew Point	**18** °C	**8** °C	**-16** °C	
Precipitation				
Precipitation	**0.0** mm	**0.0** mm	**0.0** mm	**0.00** mm
Snowdepth	-	-	-	-
Wind				
Wind	**61** km/h	**15** km/h	**0** km/h	
Gust Wind	**93** km/h	**54** km/h	**27** km/h	
Sea Level Pressure				
Sea Level Pressure	**1037** hPa	**1017** hPa	**995** hPa	

Appendix II

1st Feb – 30th May, 2017 Weather history from Almeria weather station

	Max	Avg	Min	Sum
Temperature				
Max Temperature	**33** °C	**22** °C	**14** °C	
Mean Temperature	**28** °C	**17** °C	**11** °C	
Min Temperature	**22** °C	**13** °C	**7** °C	
Degree Days				
Heating Degree Days (base 65)	13	4	0	417
Cooling Degree Days (base 65)	16	2	0	184
Growing Degree Days (base 50)	32	13	2	1546
Dew Point				
Dew Point	**19** °C	**9** °C	**-10** °C	
Precipitation				
Precipitation	**17.0** mm	**0.3** mm	**0.0** mm	**30.72** mm
Snowdepth	-	-	-	-
Wind				
Wind	**64** km/h	**14** km/h	**0** km/h	
Gust Wind	**100** km/h	**51** km/h	**23** km/h	
Sea Level Pressure				
Sea Level Pressure	**1031** hPa	**1018** hPa	**999** hPa	

Appendix III

1st July – 30th September, 2017 Weather history from Almeria weather station

	Max	Avg	Min	Sum
Temperature				
Max Temperature	**38** °C	**30** °C	**25** °C	
Mean Temperature	**32** °C	**26** °C	**20** °C	
Min Temperature	**26** °C	**22** °C	**16** °C	
Degree Days				
Heating Degree Days (base 65)	0	0	0	0
Cooling Degree Days (base 65)	24	14	4	1294
Growing Degree Days (base 50)	40	29	18	2671
Dew Point				
Dew Point	**26** °C	**19** °C	**3** °C	
Precipitation				
Precipitation	**23.1** mm	**0.4** mm	**0.0** mm	**35.05** mm
Snowdepth	-	-	-	-
Wind				
Wind	**45** km/h	**10** km/h	**0** km/h	
Gust Wind	**63** km/h	**44** km/h	**23** km/h	
Sea Level Pressure				
Sea Level Pressure	**1023** hPa	**1015** hPa	**1003** hPa	

Appendix IV
Ground control points

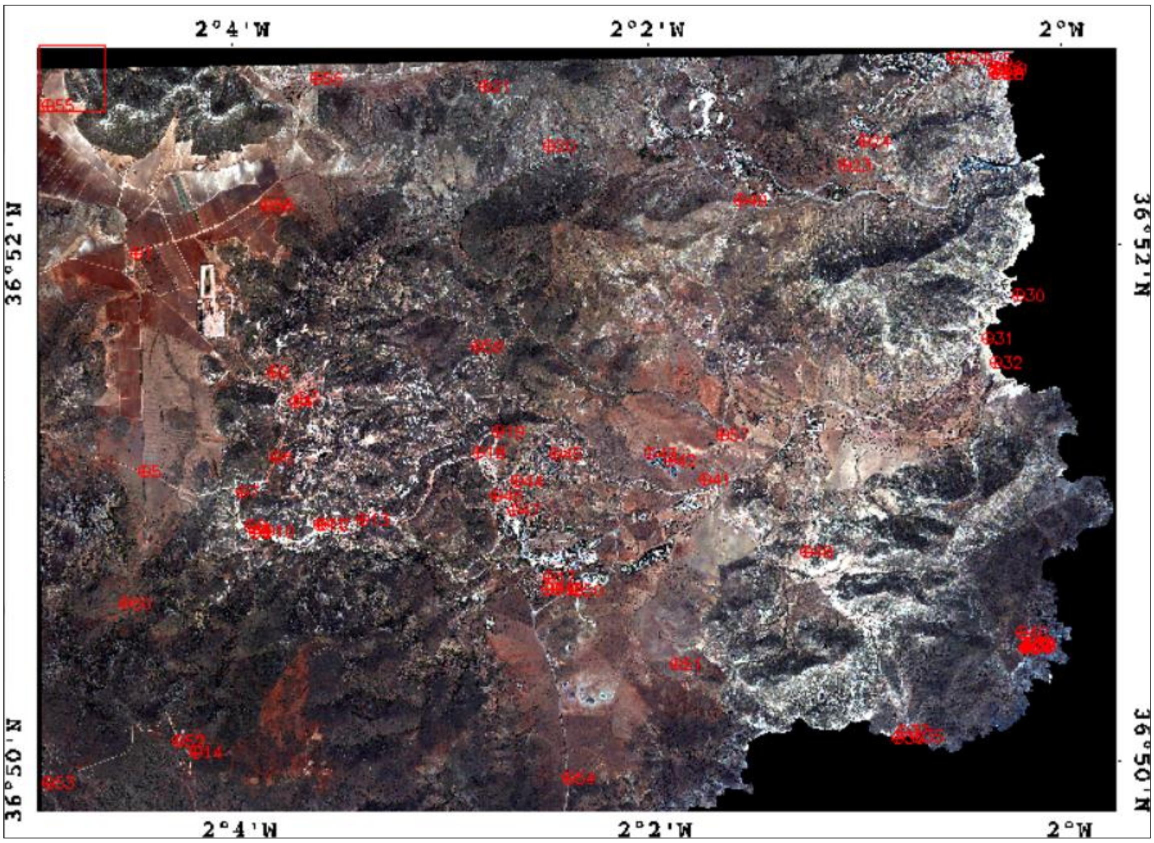

Appendix V

Waypoint and measurement locations

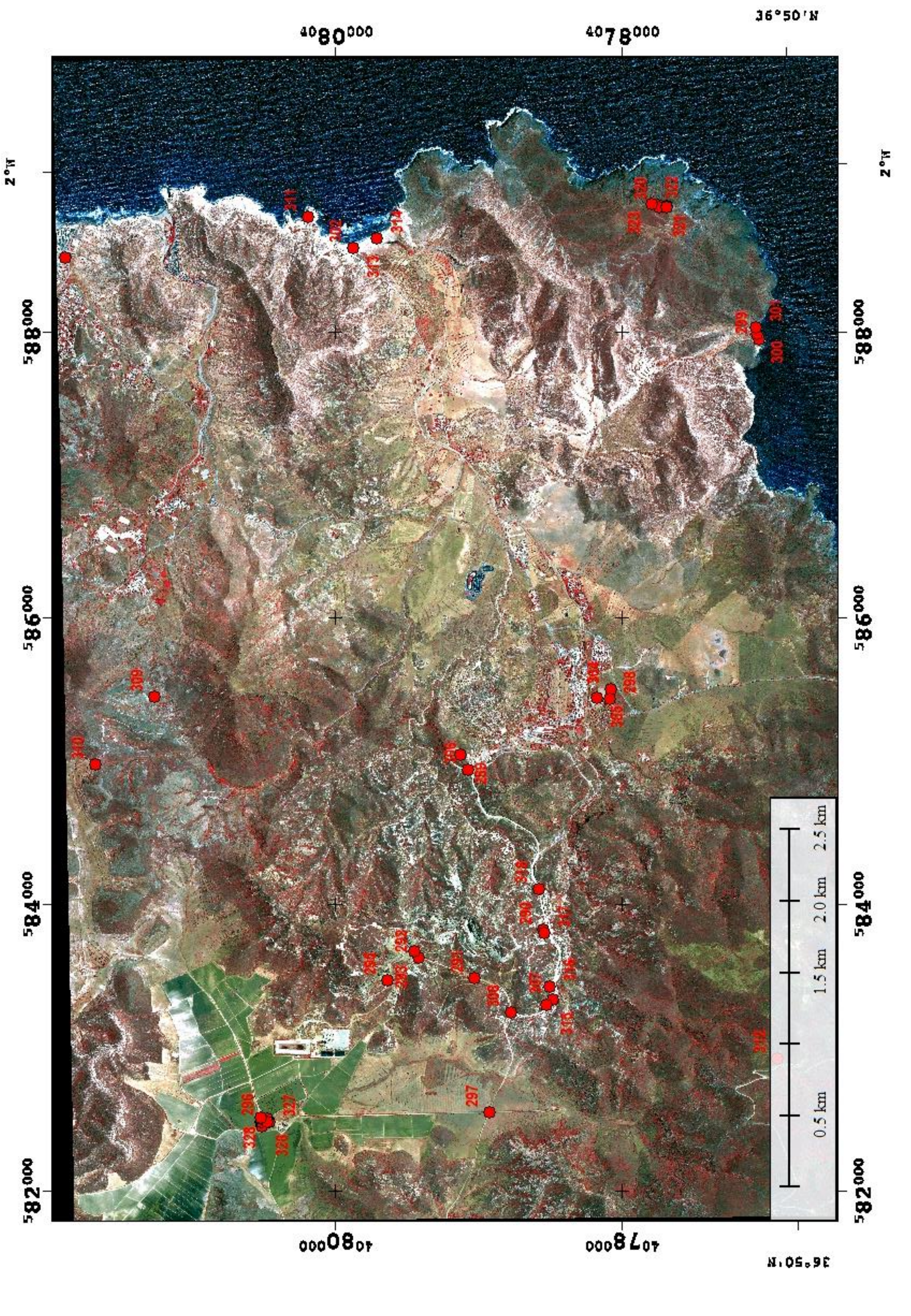

Appendix V cont…

Date	Waypoint	Easting(WGS84, utm30N)	Northing(WGS84, utm30N)	Start_photo	End_photo	Samples	Comments/description		
07/09/2017	290	583825.307	4078554.689	5751	5760	Y	Sulphur bearing/jarasite(?) spoil pile		
07/09/2017	296	582490.708	4080496.622	5774	5779	Y	Cortijo Del Fraile: Cal/Val site : bare exposed fine gravel/sand area 80 x 80 m		
07/09/2017	300	587988.136	4077059.843	5791	5795	Y	Mid point of Cala del Carnaje Beach		
07/09/2017	301	588033.343	4077069.186	5796	5798	Y	Far NE margin of Cala del Carnaje Beach		
07/09/2017	302	588585.863	4079885.425	5799	5806	Y	El Playazo Beach : 500 m wide, 50 breadth, consisting of grey/white sand; 50 m breadth btween bathers and low grassy dunes		
08/09/2017	311	588806.554	4080197.712	5846	5853	Y	Large exposure of calcareous sandstone / limestone on promontory, SE of stone fortification (El Playazo beach).		
09/08/2017	313	588591.857	4079883.38	5878	5882	Y	El Playazo beach (~WP302) : NW end of ~ 50 m traverse measuring ~ 2cm FOV with ASD hand probe		
09/08/2017	314	588655.923	4079715.406	5878	5882	Y	El Playazo beach (~WP302) : SE end of ~ 50 m traverse measuring ~ 2cm FOV with ASD hand probe		
09/08/2017	311	588806.554	4080197.712	5883	5894	Y	Large exposure of calcareous sandstone / limestone on promontory, SE of stone fortification (El Playazo beach). ~ 70 ASD random hand probe measurements within ~50m of WP311		
09/08/2017	315	583303.475	4078532.261	5895	5899	Y	Road cutting ASD hand probe traverse heading E. (Height~7m), Bearing WP315-316 bearing 100-110deg. facing S. Narrowest width : 11 m.		
09/08/2017	316	583425.318	4078509.379	5900	5904	Y	Road cutting ASD hand probe traverse heading E. (Height~5m). Narrowest width : 11 m.		
09/08/2017	290	583825.307	4078554.689			Y	ASD hand probe measurements of sulphur/jarosite(?) spoil pile.		
09/08/2017	317	583803.378	4078545.154	5905	5909	Y	Spoil pile west of WP290		
09/08/2017	315-316			5946	5979	Y	Multiple overlapping photos for merged panorama imagery.		
09/08/2017	319	583675.063	4079453.312	5980	5990	Y	Sampled mine face for possible silicified altered vertical bands		
12/09/2017	333	582481.04	4080519.161	6048	6059	Y	NW corner of bare fibre ASD grid - start of north bearing traverse. 11 measurements/grid line		
12/09/2017	334	582507.363	4080516.531	6048	6059	Y	NE corner of bare fibre ASD grid - start of north bearing traverse. 11 measurements/grid line		
12/09/2017	335	582505.084	4080484.89	6048	6059	Y	SE corner of bare fibre ASD grid - end of north bearing traverse. 11 measurements/grid line		
12/09/2017	336	582482.53	4080485.004	6048	6059	Y	SW corner of bare fibre ASD grid - end of north bearing traverse. 11 measurements/grid line		
12/09/2017	337	582512.498	4080529.34	6048	6059	Y	W edge of car		
12/09/2017	338	582512.937	4080530.01	6048	6059	Y	E edge of car		